The Astrophysical Journal, 923:119 (24pp), 2021 December 10 https://doi.org/10.3847/1538-4357/ac2c0a

GTC/CanariCam Deep Mid-infrared Imaging Survey of Northern Stars within 5 pc

Bartosz Gauza[1,2], Víctor J. S. Béjar[3,4], Rafael Rebolo[3,4,5], Carlos Álvarez[6], María Rosa Zapatero Osorio[7], Gabriel Bihain[8,9], José A. Caballero[7], David J. Pinfield[1], Charles M. Telesco[10], and Christopher Packham[11,12]
[1] Centre for Astrophysics Research, School of Physics, Astronomy and Mathematics, University of Hertfordshire, College Lane, Hatfield AL10 9AB, UK
b.gauza@herts.ac.uk
[2] Janusz Gil Institute of Astronomy, University of Zielona Góra, Lubuska 2, 65–265 Zielona Góra, Poland
[3] Instituto de Astrofísica de Canarias (IAC), Calle Vía Láctea s/n, E-38200 La Laguna, Tenerife, Spain
[4] Departamento de Astrofísica, Universidad de La Laguna (ULL), E-38205 La Laguna, Tenerife, Spain
[5] Consejo Superior de Investigaciones Científicas (CSIC), Madrid, Spain
[6] W.M. Keck Observatory, 65-1120 Mamalahoa Highway, Kamuela, HI 96743, USA
[7] Centro de Astrobiología (CSIC-INTA), Ctra. Ajalvir km 4, E-28850 Torrejón de Ardoz, Madrid, Spain
[8] Max Planck Institute for Gravitational Physics (Albert Einstein Institute), Callinstrasse 38, D-30167 Hannover, Germany
[9] Leibniz Universität Hannover, D-30167 Hannover, Germany
[10] Department of Astronomy, University of Florida, Gainesville, FL 32611, USA
[11] Department of Physics and Astronomy, University of Texas at San Antonio, San Antonio, TX 78249, USA
[12] National Astronomical Observatory of Japan, Mitaka, Tokyo 181-8588, Japan
Received 2021 March 23; revised 2021 September 24; accepted 2021 September 28; published 2021 December 15

Abstract

In this work we present the results of a direct imaging survey for brown dwarf companions around the nearest stars at the mid-infrared 10 micron range ($\lambda_c = 8.7\ \mu$m, $\Delta\lambda = 1.1\ \mu$m) using the CanariCam instrument on the 10.4 m Gran Telescopio Canarias (GTC). We imaged the 25 nearest stellar systems within 5 pc of the Sun at declinations $\delta > -25°$ (at least half have planets from radial-velocity studies), reaching a mean detection limit of 11.3 ± 0.2 mag (1.5 mJy) in the Si-2 8.7 μm band over a range of angular separations from 1″ to 10″. This would have allowed us to uncover substellar companions at projected orbital separations between ∼2 and 50 au, with effective temperatures down to 600 K and masses greater than 30 $M_{\rm Jup}$ assuming an average age of 5 Gyr and masses down to the deuterium-burning mass limit for objects with ages <1 Gyr. From the nondetection of such companions, we determined upper limits on their occurrence rate at depths and orbital separations yet unexplored by deep imaging programs. For the M dwarfs, the main component of our sample, we found with a 90% confidence level that fewer than 20% of these low-mass stars have L- and T-type brown dwarf companions with $m \gtrsim 30\ M_{\rm Jup}$ and $T_{\rm eff} \gtrsim 600$ K at ∼3.5–35 au projected orbital separations.

Unified Astronomy Thesaurus concepts: Brown dwarfs (185); Substellar companion stars (1648); Direct imaging (387); Extrasolar gaseous giant planets (509); Low mass stars (2050); Solar neighborhood (1509)

Supporting material: data behind figure

1. Introduction

High-contrast imaging surveys of stars constitute one of the foremost methods to find and study brown dwarfs and extrasolar planets. Their results complement our knowledge of these populations drawn from the objects detected by transit, radial velocity, and other techniques. Modern imaging searches extend the accessible range of the parameter space of cool companions to wider separations and longer orbital periods ($a > 5$ au, $P > 10$ yr) than those presently explored by radial velocities (RVs) or transit methods (e.g., Lafrenière et al. 2007; Biller et al. 2013; Chauvin et al. 2015a; Meshkat et al. 2015; Galicher et al. 2016; Vigan et al. 2017; Stone et al. 2018; Baron et al. 2019; Vigan et al. 2021; Launhardt et al. 2020). Moreover, directly detected brown dwarfs and planets provide a unique opportunity for spectroscopic characterization and thereby for detailed study of their fundamental physical properties, in particular their atmospheres (e.g., Gauza et al. 2015a; Skemer et al. 2016; Bonnefoy et al. 2016, 2018; Chinchilla et al. 2021).

A large number of imaging programs have thus far focused on young stars (less than 1 Gyr old) from the solar neighborhood ($d \lesssim 50$ pc), e.g., Biller et al. (2013), Lannier et al. (2016), Nielsen et al. (2019), and Vigan et al. (2021). Young nearby stars are ideal targets for direct imaging surveys because their potential substellar companions, at the early stages of evolution, are still warm and relatively bright, favoring their detection. As a consequence of both the limitations in sensitivity to the coldest companions at field ages, and the enhanced chances of detection at young ages, the most successful searches by means of confirmed detections are so far those carried out on known young stars.

The first large imaging program sensitive to substellar companions that targeted the nearest stars was the one led by Oppenheimer et al. (2001). They observed a sample of 163 northern stars in 111 star systems, located within 8 pc of the Sun using the Adaptive Optics Coronagraph on the Palomar 1.5 m telescope for the optical imaging and the Cassegrain Infrared Camera on the Palomar 5 m Hale Telescope for the near-IR. For about 80% of the surveyed stars, companions more massive than 40 $M_{\rm Jup}$ at an age of 5 Gyr would have been detected at separations between 40 and 120 au. Among the most sensitive imaging surveys of the nearest stars are those by Dieterich et al. (2012) and Carson et al. (2011). The first group

employed NICMOS on the Hubble Space Telescope to obtain high-resolution images of 255 stars within ∼10 pc, while the second used IRAC on the Spitzer Space Telescope and observed 117 targets at distances from 1.3 to 43.8 pc.

Despite several remarkable discoveries like the methane brown dwarf Gliese 229B (Nakajima et al. 1995) or the planetary system around HR 8799 (Marois et al. 2008), gas giant planets and brown dwarf companions at orbital separations beyond a few astronomical units were found to be rare by surveys of both young stars and the nearest stars. In contrast to thousands of discoveries from RV and transit methods, only a few tens of companions in or around the planetary mass regime were found by direct imaging surveys sensitive enough to detect them. Dieterich et al. (2012), from an analysis of their subsample of 138 M dwarfs, calculated a multiplicity fraction of $2.3^{+5.0}_{-0.7}$% for L- and T-type companions to M dwarfs at orbital separations of 10–70 au. The IRAC/Spitzer search performed by Carson et al. (2011) had the ability to detect 600–1100 K brown dwarf companions at semimajor axes $\gtrsim$35 au and 500–600 K companions beyond 60 au. Using Monte Carlo simulations they estimated a 600–1100 K T dwarf companion fraction of <3.4% at 35–1200 au and <12.4% for 500–600 K companions at 60–1000 au. Due to limitations in spatial resolution, contrast, and sensitivities achieved by available instruments, the orbital separations of less than 10–15 au remained largely unexplored for the presence of massive planets and brown dwarfs by the past imaging surveys.

We used the CanariCam instrument on the Gran Telescopio Canarias (GTC) to carry out deep, high spatial resolution mid-infrared imaging in the 10 micron window, targeting the nearest known stars visible from a northern site ($\delta > -25°$), to search for ultracool brown dwarfs and massive planets. We aimed to detect companions at 1″–10″ separations, which translates to 2.0–50 au, or orbital periods typically longer than 10 years. Therefore, our search extends to orbital separations and periods not explored yet by previous imaging or RV surveys. Since stars in the solar vicinity are typically old, at ages over 1 Gyr, any low-mass substellar companion will have cooled down to a $T_{\rm eff}$ well below 1000 K. At such temperatures, the maximum flux emission shifts from the near- to mid-IR. Hence, CanariCam at GTC provided an opportunity to perform a competitive search with respect to direct imaging surveys completed at the optical or near-IR using adaptive optics and coronagraphic systems, by means of being sensitive to the coolest companions. In this work we present the general results of the program. The rest of the paper is structured as follows. Section 2 sets out the observed sample of stars, Section 3 describes the observations and data processing steps, and Section 4 presents the analysis and results: relative astrometry of resolved binaries, contrast curves and sensitivities, constraints on physical parameters of detectable companions, and the upper limit estimates on the occurrence rate of companions. Section 5 contains a comparison of our results to those of other surveys and a discussion regarding the stellar binaries and known planet hosts in the sample. Conclusions and final remarks are presented in Section 6.

2. The Sample

The sample of CanariCam targets consists of the nearest known stars from the northern sky, visible from the Roque de los Muchachos Observatory, that is, with declinations $\delta > -25°$. We used the One Hundred Nearest Star Systems list provided by the Research Consortium On Nearby Stars (RECONS; Henry et al. 1997, 2006, 2018), complemented with the astrometric data from the Gaia DR2 and EDR3 (Gaia Collaboration 2018, 2021) where available, starting from the nearest star in the Northern Hemisphere, GJ 699 (Barnard's Star) and moving to more distant ones.

In total we have observed 33 individual stars within 5 pc arranged in 25 systems, five of which are double: GJ 820 A+B, GJ 15 A+B, GJ 65 AB, GJ 725 A+B, and GJ 860 AB, and two of which are triple: GJ 866 ABC and GJ 1245 ABC. We count here GJ 866 ABC as two stars, since its individual components AC were not resolved, and (AC)B were marginally resolved in our observations. Additionally, two stars, Sirius and Procyon, have known white dwarf companions. The notation "A+B" signifies that the components were observed individually as separate CanariCam targets, and "AB" that both components were observed simultaneously as a single target. The sample includes one A-, one F-, and one G-type star, three K stars, and 27 M dwarfs. Such a distribution of spectral types implies that our statistical results will be significant only for M dwarfs. The sample is a volume-limited sample complete up to 4.0 pc. We have imaged all of the 19 known stellar systems at $\delta > -25°$ within this distance, and 6 out of 15 known systems between 4 and 5 pc observable from our site. Due to observational limitations due to target brightness, substellar objects were not considered as target primaries. Hence, the Y2-type brown dwarf WISE 0855-0714 located at 2.23 ± 0.04 pc (Luhman 2014; Luhman & Esplin 2016) and the ∼500 K brown dwarf UGPS J072227.51-054031.2 at 4.12 ± 0.04 pc (Leggett et al. 2012) were not included in our sample. The remaining nine objects between 4 and 5 pc were not observed because of the limited telescope time available for the program.

Table 1 lists the observed stars, including compiled information on their equatorial coordinates at J2000 epoch (proper motions taken into account), spectral types, trigonometric parallax, distance, and proper motions. Table 2 list their near- and mid-IR photometry. Because all known stars in the solar vicinity have large and well-determined proper motions, our survey was designed to find common proper-motion companions. Any additional source detected within the field of view would have been considered as a potential companion, without any criteria based on photometric colors. Its companionship could be easily verified through second-epoch observations.

We have searched through the literature to gather the available information on the planets discovered around our sample stars by RVs, transits, and other methods, as well as constraints on the substellar companions from other surveys or signs of RV or astrometric trends indicating the possible presence of a distant companion. Notes with selected essential information regarding each star are compiled in Table A1 in the Appendix.

3. Observations and Data Processing

The program was carried out in queue-mode observations, starting in 2012 and ending in 2015. We used the mid-infrared camera CanariCam (Telesco et al. 2008) operating at the Nasmyth-A focal station of the 10.4 m Gran Telescopio Canarias (GTC) at the Roque de los Muchachos Observatory on the island of La Palma (Spain). CanariCam was designed to reach the diffraction limit of the GTC at mid-IR wavelengths (7.5–25 μm). The instrument uses a Raytheon 320 × 240 Si:As

Table 1
CanariCam Target Sample

Star	Other Name	R.A. (J2000) (hh:mm:sss)	Decl. (J2000) (dd:mm:ss)	Spectral Type	d (pc)	π (mas)	$\mu_\alpha \cos\delta$ (mas yr^{-1})	μ_δ (mas yr^{-1})
GJ 699	Barnard's Star	17:57:48.499	+04:41:36.11	M3.5	1.827 ± 0.0010	547.45 ± 0.29	-802.80 ± 0.64	$10{,}362.54 \pm 0.36$
GJ 406	CN Leo	10:56:28.826	+07:00:52.34	M6.0	2.409 ± 0.0004	415.18 ± 0.07	-3866.34 ± 0.08	-2699.22 ± 0.07
GJ 411	Lalande 21185	11:03:20.194	+35:58:11.57	M2.0	2.546 ± 0.0002	392.75 ± 0.03	-580.06 ± 0.03	-4776.59 ± 0.03
GJ 244	Sirius	06:45:08.917	−16:42:58.02	A1.0	2.670 ± 0.0017	374.49 ± 0.23	-461.57 ± 0.28	-914.52 ± 0.33
GJ 65 AB	BL Cet + UV Cet	01:39:01.453	−17:57:02.04	M5.5, M6.0	2.720 ± 0.0055	367.71 ± 0.74	3385.32 ± 0.67	544.39 ± 0.38
GJ 729	V1216 Sgr	18:49:49.364	−23:50:10.45	M3.5	2.976 ± 0.0003	336.03 ± 0.03	639.37 ± 0.04	-193.96 ± 0.03
GJ 905	HH And	23:41:55.036	+44:10:38.82	M5.0	3.160 ± 0.0004	316.48 ± 0.04	112.53 ± 0.04	-1591.65 ± 0.03
GJ 144	ϵ Eridani	03:32:55.845	−09:27:29.73	K2.0	3.220 ± 0.0014	310.58 ± 0.14	-974.76 ± 0.16	20.88 ± 0.12
GJ 447	FI Vir	11:47:44.397	+00:48:16.40	M4.0	3.375 ± 0.0003	296.31 ± 0.03	607.30 ± 0.03	-1223.03 ± 0.02
GJ 866(AC)B	EZ Aqr	22:38:36.081	−15:17:23.89	M5.0	3.406 ± 0.0105	293.60 ± 0.90	2314.8 ± 8.0	2295.3 ± 8.0
GJ 820 A	61 Cyg A	21:06:53.940	+38:44:57.90	K5.0	3.497 ± 0.0012	285.95 ± 0.10	4164.17 ± 0.19	3249.99 ± 0.25
GJ 820 B	61 Cyg B	21:06:55.264	+38:44:31.36	K7.0	3.495 ± 0.0007	286.15 ± 0.06	4105.79 ± 0.09	3155.76 ± 0.10
GJ 280	Procyon	07:39:18.119	+05:13:29.95	F5	3.507 ± 0.0079	285.17 ± 0.64	-714.59 ± 2.06	-1036.80 ± 1.15
GJ 725 A	HD 173739	18:42:46.705	+59:37:49.41	M3.0	3.523 ± 0.0003	283.84 ± 0.02	-1311.68 ± 0.03	1792.33 ± 0.03
GJ 725 B	HD 173740	18:42:46.894	+59:37:36.72	M3.5	3.523 ± 0.0004	283.84 ± 0.03	-1400.26 ± 0.04	1862.53 ± 0.03
GJ 15 A	GX And	00:18:22.885	+44:01:22.64	M1.5	3.562 ± 0.0003	280.71 ± 0.02	2891.52 ± 0.02	411.83 ± 0.01
GJ 15 B	GQ And	00:18:25.824	+44:01:38.09	M3.5	3.563 ± 0.0004	280.69 ± 0.03	2862.80 ± 0.02	336.43 ± 0.02
GJ 1111	DX Cnc	08:29:49.353	+26:46:33.63	M6.5	3.581 ± 0.0008	279.25 ± 0.06	-1113.69 ± 0.06	-612.19 ± 0.05
GJ 71	τ Cet	01:44:04.091	−15:56:14.93	G8.5	3.652 ± 0.0023	273.81 ± 0.17	-1721.73 ± 0.18	854.96 ± 0.09
GJ 54.1	YZ Cet	01:12:30.637	−16:59:56.36	M4.5	3.717 ± 0.0005	269.06 ± 0.03	1205.07 ± 0.04	637.55 ± 0.05
GJ 273	Luyten's Star	07:27:25.093	+05:12:35.63	M3.5	3.786 ± 0.0006	264.13 ± 0.04	571.23 ± 0.05	-3691.49 ± 0.04
SO 0253+16	Teegarden's Star	02:53:00.891	+16:52:52.64	M7.0	3.832 ± 0.0014	260.99 ± 0.09	3429.08 ± 0.09	-3805.54 ± 0.08
GJ 860 AB	Kruger 60 AB	22:27:59.557	+57:41:42.08	M3.0, M4.0	4.010 ± 0.0026	249.39 ± 0.16	-725.23 ± 0.54	-223.46 ± 0.35
GJ 83.1	TZ Ari	02:00:12.956	+13:03:07.02	M4.0	4.470 ± 0.0014	223.73 ± 0.07	1096.46 ± 0.07	-1771.53 ± 0.06
GJ 687	LHS 450	17:36:25.899	+68:20:20.90	M3.0	4.550 ± 0.0004	219.79 ± 0.02	-320.68 ± 0.02	-1269.89 ± 0.03
GJ 1245 ABC	LHS 3494	19:53:54.482	+44:24:51.34	M5.5, M, M6.0	4.660 ± 0.0010	214.57 ± 0.05	349.36 ± 0.06	-480.32 ± 0.05
GJ 876	IL Aqr	22:53:16.732	−14:15:49.30	M3.5	4.672 ± 0.0008	214.04 ± 0.04	957.72 ± 0.04	-673.60 ± 0.03
GJ 1002	LHS 2	00:06:43.197	−07:32:17.02	M5.0	4.846 ± 0.0011	206.35 ± 0.05	-811.57 ± 0.06	-1893.25 ± 0.03

detector with a pixel scale of 79.8 ± 0.2 mas, which covers a field of view of $25\farcs6 \times 19\farcs2$ on the sky. We imaged our targets in the 10 micron window, using a medium-band silicate filter centered at $\lambda = 8.7$ μm ($\delta\lambda = 1.1$ μm). The choice of this particular bandpass was a compromise between the instrument performance, in particular filter transmissivity, and the sky background contribution, which is significantly higher at the N broadband and other narrowband filters than at the Si-2 filter. Si-2 is also favored by a better spatial resolution, since the diffraction disk is larger at the other available narrowband filters at longer wavelengths. Observations were executed under the following restricted atmospheric conditions: spectroscopic (clear sky with possible thin cirrus) or better, i.e., photometric/clear sky transparency, precipitable water vapor (PWV) at the level of 5–12 mm and an image quality of $<0\farcs3$, corresponding to a seeing of $\sim 0\farcs8$ in the R band.

Observations were performed with the standard chopping and nodding technique used in the mid-IR to remove the sky emission and radiative offset. Chopping consists of switching the telescope secondary mirror at a typical frequency of a few (2–5) Hz between the position of the source (on-source) and the nearby sky (off-source). This rapid movement of the secondary mirror allows for subtraction of the sky background emission that is varying in time at frequencies below the chop frequency. Movement of the secondary mirror changes the optical configuration of the telescope, resulting in two different emission patterns seen by the camera and producing a spurious signal termed the radiative offset seen in the chop-differenced images. To remove the radiative offset, the telescope is moved between two nod positions to swap over on- and off-source positions.

We used an ABBA nodding sequence and "on-chip" chopping and nodding, with a chop-throw and nod offset of 8 arcsec, a chopping frequency of 1.93 or 2.01 Hz, and a nod settle time of about 45 s. The on-chip method is recommended whenever the scientific target is point-like, since both on-source and off-source chop positions contain the signal of the target inside the detector field of view and can be aligned and combined. Individual frames of 26 and 19 ms exposures were co-added by CanariCam control software to savesets of 1.6 and 6 s depending on the brightness of the source. We used an on-source integration time of 40 minutes in total, divided into two observing blocks (OBs) of 20 minutes. Each block contained three data cube files composed of a set of individual images (savesets) at subsequent chopping and nodding positions. For the two observing blocks we set the instrument at two different position angles to rotate the field of view (FOV) typically by 30° (60° and 90° rotations were also used in some cases), and adjusted the configuration of chop and nod position angles so as to maintain the chop/nod parallel to the longer axis of the detector. The use of two different orientations of instrument position angle was a way to initially check the reliability of potential faint sources, distinguish from bad pixels, and explore the region along the horizontal axis of detector, where the cross-talk of the star in the 16 channels is more evident, and the

Table 2
Near- and Mid-infrared Photometry (from 2MASS, the Wide-field Infrared Survey Explorer (WISE), and Akari S9W) of Stars in the Sample

Star	J (mag)	H (mag)	K_s (mag)	$W1$ (mag)	$W2$ (mag)	$W3$ (mag)	$W4$ (mag)	S9W (Jy)
GJ 699	5.244 ± 0.020	4.834 ± 0.034	4.524 ± 0.020	4.386 ± 0.073	3.600 ± 0.062	4.036 ± 0.016	3.921 ± 0.025	…
GJ 406	7.085 ± 0.024	6.482 ± 0.042	6.084 ± 0.017	5.807 ± 0.055	5.487 ± 0.031	5.481 ± 0.015	5.310 ± 0.031	0.38 ± 0.02
GJ 411	4.203 ± 0.242	3.640 ± 0.202	3.254 ± 0.306	3.239 ± 0.136	2.360 ± 0.071	3.045 ± 0.010	2.934 ± 0.024	3.40 ± 0.02
GJ 244	−1.391 ± 0.109	−1.391 ± 0.184	−1.390 ± 0.214	2.387 ± 0.059	0.786 ± 0.112	0.497 ± 0.018	−1.330 ± 0.005	198.0 ± 6.9
GJ 65 AB	6.283 ± 0.019	5.690 ± 0.029	5.343 ± 0.021	5.053 ± 0.072	4.575 ± 0.041	4.762 ± 0.015	4.616 ± 0.025	0.65 ± 0.01
GJ 729	6.222 ± 0.018	5.655 ± 0.034	5.370 ± 0.016	5.164 ± 0.062	4.754 ± 0.033	4.911 ± 0.014	4.715 ± 0.026	0.60 ± 0.01
GJ 905	6.884 ± 0.026	6.247 ± 0.027	5.929 ± 0.020	5.694 ± 0.056	5.410 ± 0.029	5.393 ± 0.015	5.254 ± 0.031	0.38 ± 0.01
GJ 144	2.228 ± 0.298	1.880 ± 0.276	1.776 ± 0.286	2.970 ± 0.215	2.285 ± 0.055	1.770 ± 0.006	1.288 ± 0.005	12.86 ± 0.05
GJ 447	6.505 ± 0.023	5.945 ± 0.024	5.654 ± 0.024	5.457 ± 0.064	5.012 ± 0.034	5.176 ± 0.013	5.027 ± 0.031	0.53 ± 0.01
GJ 866(AC)B	6.553 ± 0.019	5.954 ± 0.031	5.537 ± 0.020	5.314 ± 0.062	4.889 ± 0.035	5.006 ± 0.015	4.877 ± 0.030	0.56 ± 0.02
GJ 820 A	3.114 ± 0.268	2.540 ± 0.198	2.248 ± 0.318	2.822 ± 0.317	2.120 ± 0.080	2.334 ± 0.009	2.206 ± 0.011	7.00 ± 0.09
GJ 820 B	3.546 ± 0.278	2.895 ± 0.218	2.544 ± 0.328	6.224 ± 0.010	2.884 ± 0.001	2.595 ± 0.009	2.529 ± 0.013	5.95 ± 0.12
GJ 280	−0.498 ± 0.151	−0.666 ± 0.270	−0.658 ± 0.322	2.147 ± 0.397	0.625 ± 0.255	1.148 ± 0.022	−0.646 ± 0.003	109.4 ± 1.7
GJ 725 A	5.189 ± 0.017	4.741 ± 0.036	4.432 ± 0.020	4.498 ± 0.226	3.520 ± 0.157	4.070 ± 0.014	3.937 ± 0.018	2.09 ± 0.03
GJ 725 B	5.721 ± 0.020	5.197 ± 0.024	5.000 ± 0.023	5.014 ± 0.325	4.309 ± 0.206	4.588 ± 0.016	4.464 ± 0.025	2.09 ± 0.03
GJ 15 A	5.252 ± 0.264	4.476 ± 0.200	4.018 ± 0.020	3.853 ± 0.099	3.130 ± 0.074	3.707 ± 0.015	3.595 ± 0.022	1.84 ± 0.02
GJ 15 B	6.789 ± 0.024	6.191 ± 0.016	5.948 ± 0.024	5.745 ± 0.045	5.419 ± 0.028	5.463 ± 0.015	5.303 ± 0.030	1.84 ± 0.02
GJ 1111	8.235 ± 0.021	7.617 ± 0.018	7.260 ± 0.024	7.030 ± 0.031	6.819 ± 0.020	6.630 ± 0.015	6.467 ± 0.058	0.14 ± 0.01
GJ 71	2.149 ± 0.310	1.800 ± 0.234	1.794 ± 0.274	2.444 ± 0.510	1.846 ± 0.163	2.071 ± 0.011	1.671 ± 0.010	12.37 ± 0.07
GJ 54.1	7.258 ± 0.020	6.749 ± 0.033	6.420 ± 0.017	6.167 ± 0.044	5.929 ± 0.021	5.888 ± 0.014	5.719 ± 0.036	0.27 ± 0.01
GJ 273	5.714 ± 0.032	5.219 ± 0.063	4.857 ± 0.023	4.723 ± 0.074	4.108 ± 0.041	4.461 ± 0.016	4.325 ± 0.027	0.93 ± 0.01
SO 0253+16	8.394 ± 0.027	7.883 ± 0.040	7.585 ± 0.046	7.322 ± 0.027	7.057 ± 0.020	6.897 ± 0.017	6.718 ± 0.076	0.10 ± 0.01
GJ 860 AB	5.575 ± 0.027	5.038 ± 0.034	4.777 ± 0.029	4.690 ± 0.075	4.089 ± 0.037	4.299 ± 0.014	4.122 ± 0.025	1.10 ± 0.02
GJ 83.1	7.514 ± 0.017	6.970 ± 0.027	6.648 ± 0.017	6.438 ± 0.042	6.162 ± 0.021	6.100 ± 0.014	5.964 ± 0.043	0.22 ± 0.02
GJ 687	5.335 ± 0.021	4.766 ± 0.033	4.548 ± 0.021	4.397 ± 0.094	3.763 ± 0.061	4.182 ± 0.015	4.064 ± 0.018	1.16 ± 0.01
GJ 1245 AC	7.791 ± 0.023	7.194 ± 0.016	6.854 ± 0.016	6.600 ± 0.065	6.379 ± 0.025	6.244 ± 0.016	6.076 ± 0.051	…
GJ 1245 B	8.275 ± 0.026	7.728 ± 0.031	7.387 ± 0.018	7.178 ± 0.066	6.968 ± 0.029	6.853 ± 0.022	6.765 ± 0.089	…
GJ 876	5.934 ± 0.019	5.349 ± 0.049	5.010 ± 0.021	4.844 ± 0.077	4.374 ± 0.046	4.635 ± 0.014	4.538 ± 0.026	0.79 ± 0.03
GJ 1002	8.323 ± 0.019	7.792 ± 0.034	7.439 ± 0.021	7.176 ± 0.028	6.993 ± 0.020	6.860 ± 0.016	6.766 ± 0.080	0.14 ± 0.02

Table 3
CanariCam Observation Log

Star	OB #	Observation Date	MJD	Saveset (s)	On-source (s)	Instr. PA	Chop PA	Nod PA	Readout type	Sky	PWV (mm)
GTC4-12BGCAN, Semester: 2012B											
GJ 1111	01	2012-12-26	56287.267541	5.96	3 × 404	0	90	−90	S1R1-CR	Ph	∼7.1
	02	2012-12-28	56289.211395	5.96	3 × 404	300	150	−30	S1R1-CR	Ph	∼4.2
GJ 71	03	2012-09-29	56199.097535	5.96	3 × 404	1.83	90	−90	S1R1-CR	Ph	<9.1
	04a	2012-09-29	56199.138148	5.96	1 × 404	1.83	90	−90	S1R1-CR	Ph	<9.1
	04a1	2012-10-05	56205.036337	5.96	3 × 404	300	150	−30	S1R1-CR	L.Cs.	9.0
	04a2	2012-12-03	56264.907141	5.96	1 × 404	0	150	−30	S1R1-CR	Cl	6.3
GJ 406	05	2012-12-04	56265.186042	1.49	3 × 454	0	90	−90	S1R1-CR	Cl	6.0
	06	2013-01-29	56321.090712	1.49	3 × 454	300	150	−30	S1R1-CR	Ph	5.5–5.7
	06a1	2012-12-04	56265.283756	1.49	2 × 454	0	150	−30	S1R1-CR	Cl	6.7
	06a2	2012-12-28	56289.257245	5.96	3 × 404	300	150	−30	S1R1-CR	Ph	<5.0
GJ 144	07	2012-09-29	56199.208941	5.96, 1.49	404, 545, 378	1.83	90	−90	S1R1-CR	Ph	<9.1
	08	2012-10-05	56205.085058	1.49	4 × 454	300	150	−30	S1R1-CR	L.Cs.	9.0
GTC9-12AGCAN, Semesters: 2012AB, 2013AB											
GJ 820 A	01	2013-09-05	56540.063970	1.55	3 × 432	0	90	−90	S1R3	Ph	7.7–8.9
	02	2013-09-05	56540.114497	1.55	3 × 432	300	30	−150	S1R3	Ph	8.3–8.6
GJ 699	05	2012-07-29	56137.973895	5.96	3 × 404	0	−90	90	S1R1-CR	Ph	8.6–9.3
	06	2012-07-30	56138.020220	5.96	3 × 404	90	−180	0	S1R1-CR	Ph	8.6–9.3
	19	2013-06-09	56452.160365	1.55	3 × 432	0	90	−90	S1R3	Ph	6.7
	20	2013-06-10	56453.185434	1.55	3 × 360	300	0	180	S1R3	Ph	6.7
GJ 729	09	2013-09-05	56540.897378	1.55	3 × 432	0	90	−90	S1R3	Ph	8.7–9.2
	10	2013-09-14	56549.853825	1.55	3 × 432	330	60	−120	S1R3	Cl	9.9–9.2
GJ 905	11	2013-06-07	56450.190631	6.21	3 × 417	0	90	−90	S1R3	Ph	6.3
	12	2013-06-08	56451.191418	6.21	3 × 417	300	−180	0	S1R3	Ph	7.2
GJ 15 A	15	2012-12-27	56288.852112	5.96	3 × 404	0	90	−90	S1R1-CR	Ph	∼4.6
	16	2012-12-27	56288.916597	5.96	1211	90	−180	0	S1R1-CR	Ph	4.6
GJ 15 B	17	2012-12-28	56289.825174	5.96	3 × 404	0	90	−90	S1R1-CR	Ph	<5.5
	18	2012-12-28	56289.867014	5.96	3 × 404	0	−180	0	S1R1-CR	Ph	<6.0
GJ 54.1	21	2013-08-30	56534.128715	6.21	3 × 417	0	90	−90	S1R3	Ph	4.7–5.0
	22	2013-08-30	56534.173160	6.21	4 × 417	0	90	−90	S1R3	Ph	5.0–5.2
GJ 65 AB	26	2013-09-15	56550.091308	1.55	3 × 432	0	90	−90	S1R3	Cl	<12
	27	2013-09-15	56550.160683	1.55	3 × 432	330	60	−120	S1R3	Cl	9.9–12
GJ 866 (AC)B	29	2013-09-08	56543.051701	1.55	3 × 432	330	60	−120	S1R3	Cl	9.0–10.3
GJ 280	30	2014-01-04	56661.065336	1.55	3 × 432	0	90	−90	S1R3	Cl	7.9–9.1
	31	2014-01-04	56661.143403	1.55	3 × 432	330	60	−120	S1R3	Cl	8.3–9.4
GJ 725 A	32	2013-09-05	56540.951082	1.55	3 × 432	0	90	−90	S1R3	Ph	8.7–9.2
	33	2013-09-05	56540.996568	1.55	3 × 432	330	60	−120	S1R3	Ph	8.4–9.1
GJ 725 B	34	2013-09-08	56543.926146	1.55	3 × 432	0	90	−90	S1R3	Cl	8.1–9.1
	35	2013-09-08	56543.976256	1.55	3 × 432	330	60	−120	S1R3	Cl	8.7–9.0
GTC8-14AGCAN, Semesters: 2014AB, 2015AB											
GJ 411	01	2015-02-01	57054.289022	1.55	2 × 432, 360	0	90	−90	S1R3	Sp	∼8
	02	2015-02-03	57056.005301	1.55	3 × 432	330	60	−120	S1R3	Cl	6.0
	39	2015-06-03	57176.938229	1.55	3 × 432	0	90	−90	S1R3	Cl	10.8–12.2
GJ 244	03	2015-02-06	57059.926707	1.55	3 × 432	0	90	−90	S1R3	Sp	13.3
	04	2015-02-01	57054.923368	1.55	2 × 432, 360	330	60	−120	S1R3	L.Cs.	7.0
GJ 447	05	2014-05-10	56787.896094	6.21	3 × 417	0	90	−90	S1R3	Cl	6.1–8.5
	06a	2016-01-05	57392.188420	6.21	3 × 417	30	60	−120	S1R3	Cl	5.2–6.6
GJ 15 A	09	2014-09-08	56908.079543	1.55	3 × 432	0	−90	90	S1R3	Ph	7.5
	10	2014-09-08	56908.129653	1.55	3 × 432	330	−120	60	S1R3	Ph	7.5
GJ 15 B	11	2014-09-23	56923.122396	1.55	4 × 432	0	90	−90	S1R3	Cl	7.0
	11a	2014-09-08	56908.178374	1.55	2 × 432	0	−90	90	S1R3	Ph	7.5
	12	2014-09-23	56923.191435	1.55	360, 2 × 432	330	60	−120	S1R3	Cl	7.0
GJ 65 AB	13	2014-12-02	56993.926748	1.55	3 × 432	0	90	−90	S1R3	Ph	4.7
	14	2014-12-03	56994.886817	1.55	2 × 432, 360	330	60	−120	S1R3	Ph	6.2–7.0
GJ 820 B	15	2014-06-11	56819.217245	1.55	2 × 432, 360	0	90	−90	S1R3	Ph	10.8–11.1
	16	2014-06-12	56820.185712	1.55	3 × 432	330	60	−120	S1R3	Ph	12.8–13.6
GJ 866 (AC)B	17	2014-09-22	56922.996505	1.55	3 × 432	0	90	−90	S1R3	Cl	∼6.0

Table 3
(Continued)

Star	OB #	Observation Date	MJD	Saveset (s)	On-source (s)	Instr. PA	Chop PA	Nod PA	Readout type	Sky	PWV (mm)
	18	2014-09-23	56923.051458	1.55	3 × 432, 360	330	60	−120	S1R3	Cl	7.0
GJ 144	19	2014-10-04	56934.128079	1.55	2 × 432, 360	0	90	−90	S1R3	Ph	9.7–10.6
GJ 729	20	2014-07-10	56848.043125	1.55	3 × 432	330	60	−120	S1R3	Ph	4.5–5.8
GJ 273	21	2014-03-13	56729.891626	1.55	3 × 432	0	90	−90	S1R3	Sp	<10
	22	2014-03-13	56729.997425	1.55	3 × 432	330	60	−120	S1R3	Sp	<10
GJ 860 AB	23	2014-09-02	56902.981678	6.21	417, 348, 209	0	90	−90	S1R3	Cl	12–14
	24	2014-09-03	56903.016580	6.21	278, 2 × 417, 487	0	60	−120	S1R3	Cl	12–14
SO0253+13	30	2015-02-02	57055.942853	1.55	2 × 432, 360	0	60	−120	S1R3	T.Cs.	6.0
	29_2	2015-08-28	57262.166314	6.21	209, 2 × 487, 417	0	90	−90	S1R3	Cl	6.5–7.4
	30_2	2015-09-02	57267.227269	6.21	2 × 417, 348	0	60	−120	S1R3	Cl	n.a.
GJ 83.1	47	2015-08-25	57259.131956	6.21	3 × 417	0	90	−90	S1R3	Cl	9.5.
	48a	2015-08-25	57259.180666	6.21	3 × 417	330	60	−120	S1R3	Cl	9.3–9.9
	48	2015-08-27	57261.200226	6.21	3 × 417	330	60	−120	S1R3	Cl	5.5
GJ 687	49	2015-08-22	57256.935787	1.55	3 × 432	0	90	−90	S1R3	Ph	8.4
	50a	2015-08-22	57256.986562	1.55	3 × 432	330	60	−120	S1R3	Ph	7.8–8.7
	50	2015-08-24	57258.972818	1.55	2 × 432, 360	330	60	−120	S1R3	Cl	7.6–9.7
GJ 1245	51	2015-08-19	57253.955602	6.21	3 × 417	0	90	−90	S1R3	Cl	10.1–10.8
	52	2015-08-19	57254.003559	6.21	3 × 417	330	60	−120	S1R3	Cl	10.8–12.2
GJ 876	53	2015-08-25	57259.022564	1.55	2 × 432, 360	0	90	−90	S1R3	Cl	8.0–9.0
	54	2015-08-25	57259.067002	1.55	2 × 432, 360	330	60	−120	S1R3	Cl	8.2–9.5
GJ 1002	55	2015-08-07	57241.139595	6.21	4 × 417	0	90	−90	S1R3	Cl	7.8
	56	2015-09-16	57281.062135	6.21	3 × 417	330	60	−120	S1R3	Ph	7.9–8.5

Note. Sky conditions: Ph—photometric, Cl—clear, Sp—spectroscopic, L.Cs.—light cirrus, T.Cs.—thick cirrus.

areas otherwise obscured by the negative off-source chops. A detailed observation log is presented in Table 3.

CanariCam images are stored in the standard multi-extension FITS files, with a structure of [320, 240, 2, M][N], where 320 and 240 are the image pixel dimensions, 2 is the number of chop positions, M of savesets, and N of nod positions. The data were processed using a set of dedicated `IRAF/PyRAF`[13] scripts developed within our group.

As a first step, the off-source savesets, where the star is not located at the center of the detector, were subtracted from the corresponding on-source savesets, for respective nod beam position. These chop-/sky-subtracted frames, where the star is located at the center of the detector, were then aligned to correct for relatively small misalignments (typically of less than five pixels) with respect to the preliminary shifts computed from the chop and nod pointing offsets. Then each pair of frames corresponding to the A and B nod positions was combined, to subtract the radiative offset. The sky-subtracted frames were multiplied by −1 to recover the negative contributions of the star (off-source position of the secondary mirror).

Because the negatives in the A and B nod positions do not overlap, being at opposite sides and at 8 arcsec of the on-source central location, they were also combined to subtract the radiative offset before they were aligned. Residual detector levels constant along single columns or lines but varying across these remained in both the positive and negative chop- and nod-subtracted frames; these were background fitted (masking the target) and subtracted.

The alignment itself was applied at once, to all (positive and negative) images of consecutive repetitions of an OB, relative to a same reference image, and so that the centroids of the target in all images including the reference image were shifted to the same integer pixel position value. Therefore, the ulterior alignment and combination, even with other epochs, were simplified to integer pixel shifts, obviating the need of reinterpolation. Before aligning, the images were copied into larger ones to avoid the trimming of outer data regions. Then the frames were average-combined per repetition using a shallow sigma upper and lower clipping to discard occasional short transients and sharp outliers.

Each combination involved masking the negative counts of the target. Horizontal patterns of cross-talk features, apparent for the brightest targets, were removed. Repetitions from OBs acquired with position angles differing from the North-up East-left orientation were resampled to a common orientation using the `mscimage` task. For the combination of the stacks of the different OBs, the repetitions were flux-scaled according to their zero-point magnitude—as measured on the target—and weighted inversely proportional to the scaled variance of their background noise and the square of the FWHM of the target.

A final processed image mosaic of one of the target stars, GJ 15A, with a total on-source time of 86 min is displayed in Figure 1. The counts are represented in linear scale and within $\pm 7\sigma$ of the background level, where σ is the standard deviation of the background noise. The central region with the highest sensitivity, where the sky areas of stacked frames overlap, covers a rectangle of approximately $25'' \times 19''$ ($\sim 89 \times 67$ au at

[13] `PyRAF` is a product of the Space Telescope Science Institute, which is operated by AURA for NASA.

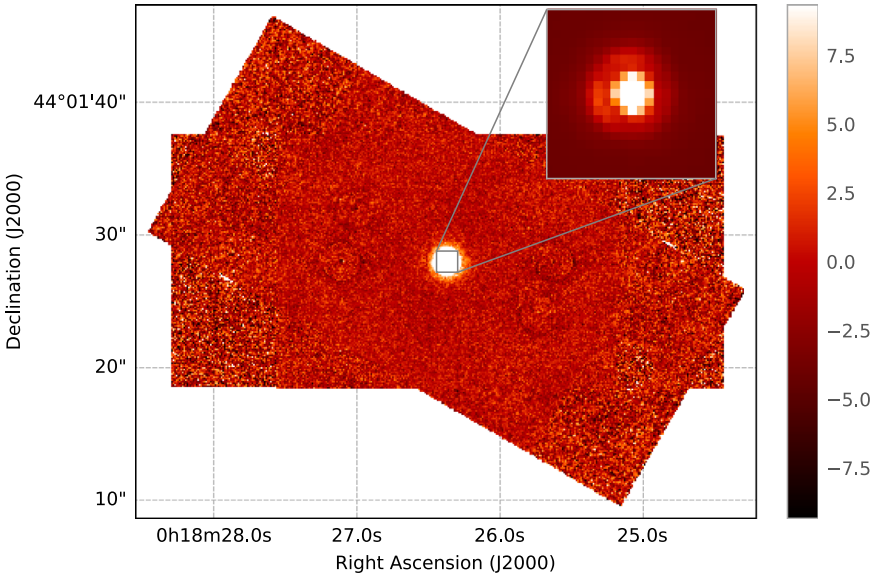

Figure 1. The final 8.7 μm image mosaic of one of the target stars, GJ 15A, encompassing the full area covered by the CanariCam data. Counts are in linear scale and in the range $\pm 7\sigma$ relative to the zero background. The deepest central region, where the stack areas overlap, is a rectangle of $\sim 25'' \times 19''$. A zoomed-in inset of $1\farcs5 \times 1\farcs5$ shows the core of the point-spread function with the first Airy disk visible. North is up and east is to the left.

(The data used to create this figure are available.)

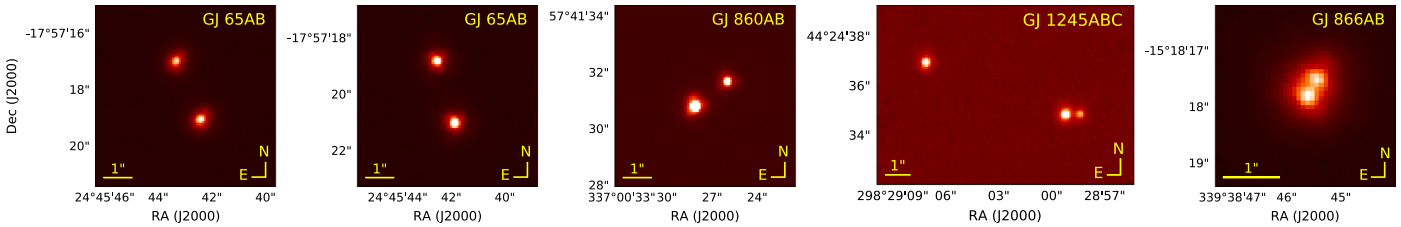

Figure 2. Images of the resolved binary and multiple stars: GJ 65AB (at two different epochs), GJ 860AB, GJ 1245ABC, and GJ 866(AC)B at the first epoch, 2013 September 8. A $1''$ scale is indicated. North is up and East is to the left.

the distance of GJ 15A). A collection of the processed CanariCam images of all of the observed stars is presented in Figures B1 and B2 in the Appendix. Figure B1 contains a set of common size ($25\farcs6 \times 19\farcs2$) central parts of the images, with the highest sensitivity and smooth background levels, whereas Figure B2 includes full FOV mosaics. All of the reduced image stacks are available at https://cloud.iac.es/index.php/s/kT3cCdP9Wxw92gZ.

4. Analysis and Results

4.1. Relative Astrometry of Resolved Binaries

As part of our CanariCam observations, we resolved the components of the binary stars GJ 65AB and GJ 860AB and the triple systems GJ 1245ABC and GJ 866(AC)B. Cut-out images of these systems are displayed in Figure 2. We measured the relative angular separations and position angles (ρ, θ) of the resolved components. Observations of GJ 65AB and GJ 866(AC)B were repeated at two separate epochs, about 1.2 and 1.0 yr apart, respectively. In case of GJ 866, the A and C pair is a spectroscopic binary (Delfosse et al. 1999; Woitas et al. 2000) at $\rho \sim 0\farcs01$, and thus only the B component was resolved in the first epoch. In the second epoch the components got closer by their orbital motion, to a separation below the angular resolution of $0\farcs298$ achieved on the images. Sirius B was marginally detected at $\rho \sim 10\farcs3$, $\theta \sim 77\fdg7$, but its low signal-to-noise ratio ($S/N \sim 4$) precludes more accurate measurements.

Table 4
Relative Astrometry of Resolved Binary/multiple Stars

Star	Epoch (MJD)	ρ ($''$)	θ ($^\circ$)
GJ 65AB	56550.125995	2.240 ± 0.012	22.94 ± 0.39
	56994.406782	2.267 ± 0.010	16.27 ± 0.35
GJ 860AB	56902.999129	1.4338 ± 0.0036	307.61 ± 0.33
GJ 866(AC)B	56543.051701	0.33 ± 0.02	331.65 ± 1.90
	56922.996505	<0.298	...
GJ 1245AB	57253.979581	6.0063 ± 0.0080	69.63 ± 0.16
GJ 1245AC	57253.979581	0.582 ± 0.007	271.26 ± 0.73

We obtained centroids of the sources using the `IRAF imcentroid` task, and transformed the X and Y pixel coordinates with their respective errors into angular separations and North-to-East position angles using the CanariCam pixel scale of 79.8 ± 0.2 mas (http://gtc.iac.es/instruments/canaricam/canaricam.php) and the orientation given by the instrument position angle in the image header. We checked that the precision of this orientation is better than $0\fdg3$ by inspecting the alignment of the chopping-nodding throw with the detector X axis. We did not perform any calibration observations. Therefore, in the determination of the relative astrometry we relied on the default internal calibration of the instrument position angle and pixel scale. Measured values are listed in Table 4.

Table 5
Detection Limits of the CanariCam Search

Star	FWHM (pix)	FWHM (″)	Determined Si-2 (mag)	Detection Limit Si-2 (mag)	M_{Si2} (mag)	$M_{min,comp}$ (M_{Jup})	$T_{eff,min,comp}$ (K)	s (au)
GJ 699	3.07	0.246	4.12 ± 0.19	11.68 ± 0.19	15.37 ± 0.19	15.0 ± 2.0	400 ± 30	3–18
GJ 406	3.25	0.260	5.59 ± 0.23	11.97 ± 0.23	15.08 ± 0.24	19.5 ± 2.0	450 ± 30	3–24
GJ 411	3.24	0.259	3.03 ± 0.13	10.75 ± 0.13	13.72 ± 0.14	29.0 ± 3.0	570 ± 40	5–25
GJ 244	3.24	0.259	-1.32 ± 0.10	10.05 ± 0.14	12.95 ± 0.15	40.0 ± 3.0	740 ± 50	18–26
GJ 65AB	3.38	0.270	5.69 ± 0.19	11.26 ± 0.19	14.13 ± 0.21	25.0 ± 2.0	520 ± 30	3–27
GJ 729	3.47	0.278	4.97 ± 0.19	10.73 ± 0.19	13.37 ± 0.20	35.0 ± 4.0	650 ± 20	4–30
GJ 905	2.99	0.239	5.49 ± 0.19	11.87 ± 0.19	14.37 ± 0.19	23.0 ± 2.0	490 ± 25	3–32
GJ 144	3.91	0.313	1.67 ± 0.19	10.70 ± 0.19	13.16 ± 0.19	37.0 ± 3.0	680 ± 50	7–32
GJ 447	3.96	0.317	5.01 ± 0.22	10.20 ± 0.22	12.57 ± 0.23	46.5 ± 5.0	830 ± 40	3–34
GJ 866(AC)B	4.40	0.352	5.13 ± 0.22	11.13 ± 0.22	13.43 ± 0.25	32.5 ± 4.0	600 ± 60	4–35
GJ 820A	2.95	0.236	2.37 ± 0.08	11.50 ± 0.08	13.79 ± 0.08	28.0 ± 1.5	560 ± 20	7–35
GJ 820B	3.15	0.252	2.67 ± 0.21	11.24 ± 0.21	13.52 ± 0.21	31.0 ± 3.5	600 ± 50	6–35
GJ 280	6.90	0.552	1.07 ± 0.25	11.01 ± 0.25	13.29 ± 0.26	36.0 ± 4.0	670 ± 60	25–35
GJ 725A	2.99	0.239	4.21 ± 0.14	11.45 ± 0.14	13.72 ± 0.15	29.0 ± 2.0	570 ± 25	4–35
GJ 725B	3.15	0.252	4.71 ± 0.17	11.45 ± 0.17	13.71 ± 0.18	29.0 ± 2.5	570 ± 30	5–35
GJ 15A	2.83	0.226	3.80 ± 0.06	11.88 ± 0.06	14.11 ± 0.06	25.0 ± 1.0	520 ± 15	4–36
GJ 15B	3.00	0.240	5.55 ± 0.09	11.84 ± 0.09	14.07 ± 0.10	25.5 ± 1.5	530 ± 15	4–36
GJ 1111	3.79	0.303	6.70 ± 0.05	11.50 ± 0.06	13.70 ± 0.08	29.0 ± 3.0	570 ± 45	3–36
GJ 71	3.58	0.286	1.78 ± 0.26	11.18 ± 0.26	13.37 ± 0.26	35.0 ± 5.0	650 ± 70	10–37
GJ 54.1	3.72	0.298	5.96 ± 0.23	11.05 ± 0.23	13.20 ± 0.25	36.5 ± 4.0	680 ± 60	3–37
GJ 273	3.23	0.258	4.48 ± 0.11	10.50 ± 0.11	12.63 ± 0.12	47.0 ± 2.5	850 ± 40	4–19
SO 0253+16	4.22	0.338	6.96 ± 0.03	10.83 ± 0.03	12.90 ± 0.04	40.0 ± 1.5	740 ± 20	3–39
GJ 860AB	3.22	0.258	4.82 ± 0.10	11.08 ± 0.10	13.05 ± 0.11	38.5 ± 2.0	710 ± 30	5–40
GJ 83.1	4.19	0.335	6.17 ± 0.28	11.26 ± 0.28	13.02 ± 0.31	38.5 ± 5.0	710 ± 75	4–44
GJ 687	3.30	0.264	4.31 ± 0.13	11.23 ± 0.13	12.95 ± 0.14	40.0 ± 3.0	740 ± 50	5–45
GJ 1245ABC	3.40	0.272	6.90 ± 0.14	11.10 ± 0.14	12.81 ± 0.15	41.5 ± 3.5	760 ± 55	5–45
GJ 876	3.22	0.258	4.76 ± 0.14	11.20 ± 0.14	12.86 ± 0.15	40.5 ± 3.0	740 ± 40	5–47
GJ 1002	3.98	0.318	6.89 ± 0.04	10.88 ± 0.04	12.52 ± 0.08	47.0 ± 2.5	850 ± 35	4–47

Note. M_{Si2}—absolute Si-2 magnitude of an object corresponding to the detection limit, $M_{min,comp}$; $T_{eff,min,comp}$—lower limits on mass and effective temperature of detectable companions; s—range of projected physical separations at which detection limits and minimum M_{comp} and T_{eff} apply.

4.2. Contrast Curves and Achieved Sensitivities

Since our observations have a bright star at the center, by aligning the individual chop-subtracted frames we could improve the resulting FWHM as compared to straight stacking of images done by default by the automatic data reduction pipeline of the instrument provided by the observatory, and to some extent compensate for the lack of a fast-guiding mode of the telescope. The mean FWHM of the point-spread functions (PSFs) of all images is 0.″28 (3.5 pixels), with the best and the worst values of 0.″23 (2.8 pixels) and 0.″55 (6.9 pixels), respectively. The quality of our data is close to the theoretical FWHM of the diffraction-limited PSF, which for GTC is 0.″23 at 8.7 μm.

We measured the detection limits on the deepest region of the final images of each target in the survey by using the ratio of the peak counts of the star to three times the background noise (σ). To determine the 3σ limiting magnitudes of the images we estimated the magnitudes of the sample stars in the Si-2 filter, using the JHK_s photometry from the 2MASS and Wide-field Infrared Survey Explorer (WISE) W1, W2, W3, and W4 photometry from the All-Sky and AllWISE Source Catalogs (Wright et al. 2010). In cases where the mid-IR photometry from WISE was highly affected by saturation, we used other measurements available in the literature from Spitzer/IRAC and the Akari S09W and L18W bands (Murakami et al. 2007). We converted the 2MASS and WISE magnitudes into fluxes using the corresponding Vega zero-points and their errors for each band from Cohen et al. (2003) and Jarrett et al. (2011). Then, we fitted a power function $f(\lambda) = c_1\lambda^{c_2} + c_3$ to the available measurements via a least-squares method and used the obtained parameters to estimate the average flux at $\lambda = 8.7$ μm. This approach does not take into account the different spectral types. However, we checked that the effect on the estimated magnitudes at this wavelength is negligible relative to overall uncertainties. The Si-2 magnitude of each star was calculated using the Vega system zero-point determined for this CanariCam filter. For Sirius A (GJ 244) we used directly the well-calibrated Si-2 flux within the standard filters from Gemini/T-ReCS observations (Skemer & Close 2011). For tight binary stars in the sample resolved by CanariCam but unresolved by WISE, the magnitudes of individual components were decomposed from the integrated magnitudes and peak-to-peak flux ratios. The values of FWHMs and Si-2 3σ detection limits for individual targets are listed in Table 5.

To measure the sensitivity as a function of angular separation from the central star, we computed the background noise, σ, as a function of radial separation from the star, by measuring the standard deviation in 1 pixel wide concentric annuli around it. The 3σ noise counts were converted to a contrast (difference in magnitude between the primary star and the measured quantity, noise in this case) by relating to the peak pixel value of the star's PSF. Results of this method were found to be consistent with a more realistic procedure based on inclusion of artificial sources, as in the analysis of the Barnard's Star data described in Gauza et al. (2015b). Then, the sensitivity limit was

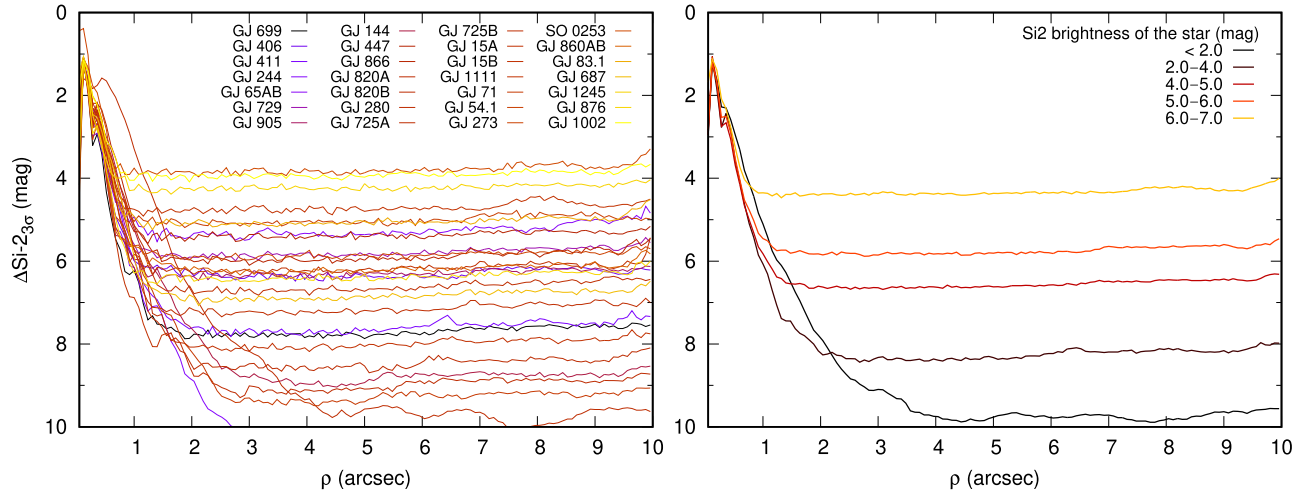

Figure 3. Left: Si-2 (8.7 μm) contrast curves at the 3σ level for all individual targets. The curves are ordered and color coded by distance of the star (as in Table 5). Right: the mean contrast curves per given interval of brightness of the stars.

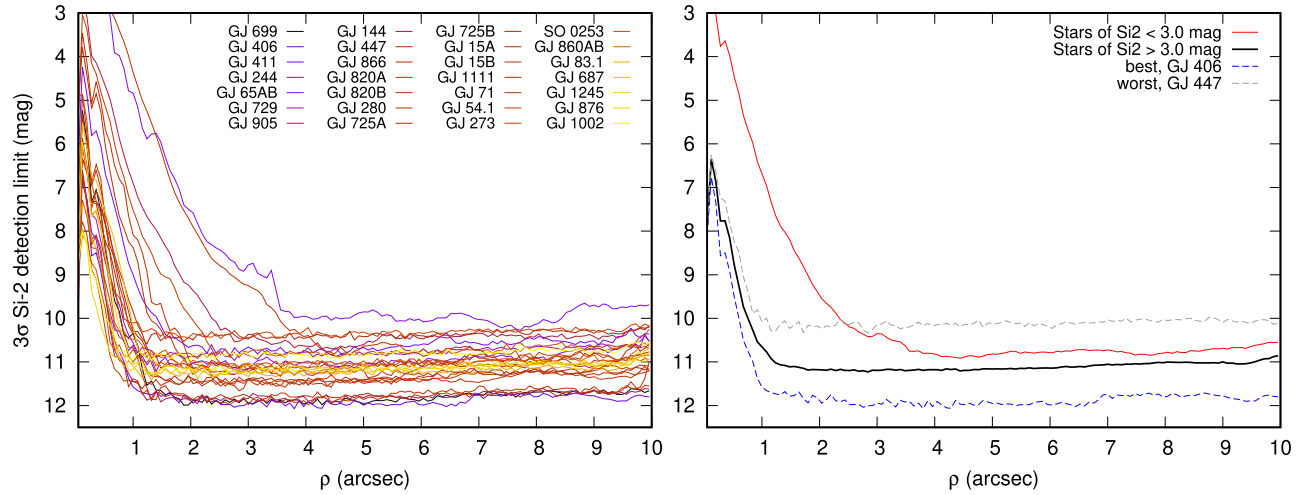

Figure 4. CanariCam Si-2 band (8.7 μm) detection limits. For each individual star in the left panel, and in the right panel, average curves for stars brighter and fainter than Si-2 = 3.0 mag, and the best (GJ 406) and the worst (GJ 447) cases.

calculated using the corresponding Si-2 magnitude of a given star.

The set of graphs of Figures 3 and 4 comprises the 3σ contrast curves and detection limit curves of the survey. The left plot of Figure 3 collects the contrast curves (ΔSi-2 mag as a function of angular separation ρ) for all observed stars individually. On the right graph are plotted the average achieved contrast versus separation, for a given brightness range of the target stars. For the brightest stars with Si-2 < 2.0 mag the maximum dynamic range, of about 10 mag, is achieved at $\sim 3''$. For stars fainter than 4.0 mag (20 stars of the sample) the maximum contrast is reached at 1.0–1.5$''$. The detection limit curves for each observed star are plotted in the left panel of Figure 4. In the right panel, we plot the mean detectability curves for stars brighter and fainter than 3.0 mag, and also the best and the worst cases, which were for GJ 699 and GJ 273, respectively. For most of the observed stars ($\sim$80%), i.e., those with Si-2 < 3.0 mag, the detectability limit of Si-2 $= 11.3 \pm 0.2$ mag, on average, was reached at $\rho \gtrsim$ 1.0–1.5$''$ separation.

For eight targets (GJ 699, GJ 65AB, GJ 729, GJ 144, GJ 447, GJ 866, GJ 15A, and GJ 15B), observations were performed at two epochs separated by $\sim$1.0–1.7 yr. In these cases, the orbital motion of companions may not be negligible. We estimate, considering a 20–40 $M_{\rm Jup}$ companion in a circular, face-on orbit, that the angular shift induced by orbital motion becomes significant, i.e., exceeds the average spatial resolution of the images, for $a \lesssim$ 8.0–16.5 au orbits, corresponding to $\rho \lesssim 2''.0$–$6''.5$ angular separations at $d = 2.5$–3.5 pc. Stacking of images of well-separated epochs would result in either a smearing of or point-source doubling for any potential close-in faint companion. In any case, we searched over these closest separations around those stars in the stacks of two epochs' observations both combined together and separately. The contrast curves and detection limits reported for these targets were computed on single-epochs image stacks.

4.3. Constraints on Substellar Companions

We did not find any new companions to the stars imaged in this survey. All of the final processed images were examined by us for the presence of faint, point-like sources directly by a visual inspection. We searched for candidate objects on images of all of the available CanariCam data combined, as well as on images stacked separately at different observing epochs or at

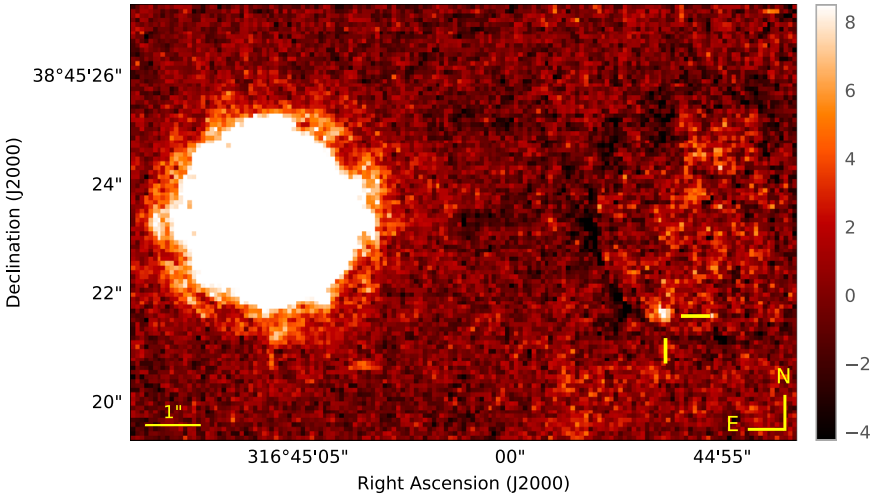

Figure 5. CanariCam image of GJ 820A and the faint (Si-2 $\sim$ 10.4 mag) source detected at $\rho = 7\overset{''}{.}20 \pm 0\overset{''}{.}04$, $\theta = 256\overset{\circ}{.}2 \pm 0\overset{\circ}{.}3$ (epoch J2013.75), indicated by two yellow lines. The faint source is the background star TYC 3168-590-1.

different orientations of instrument position angle (typically contained in two separate observing blocks of a half of the total on-source time available). We also looked for candidates in the regions masked by the negatives by using the complementing images. We did not employ any PSF subtraction method because adjusting the image display contrast is sufficient to efficiently inspect the immediate surroundings of the target stars even to one FWHM separation of the stellar PSF.

Only one additional faint source was detected within the field of view on the images of GJ 820A (displayed in Figure 5). It was detected in both OBs taken with different instrument position angles (North-to-East sky orientation rotated by 60°), with an apparent magnitude of 10.4 ± 0.3 in the Si-2 band, at an angular separation and position angle of $\rho = 7.20 \pm 0.04$ arcsec and $\theta = 256\overset{\circ}{.}2 \pm 0\overset{\circ}{.}3$, respectively. We calculated its equatorial coordinates at the epoch of the CanariCam observation based on the precise proper motion of GJ 820A and the measured ρ and θ. Using available archival observations and catalogs of this area of the sky, we found that the source is the background star TYC 3168-590-1 (2MASS J21065820 +3845411) with $V_T = 10.737 \pm 0.066$, $J = 10.669 \pm 0.024$, $H = 10.466 \pm 0.016$, and $K_s = 10.405 \pm 0.013$ mag. It is also cataloged in Gaia EDR3 with $G = 11.517 \pm 0.003$ mag and a parallax of 2.51 ± 0.01 mas. Apart from this source, no other additional sources were identified. In this section we translate the detection limits of each star to constraints on the physical properties of detectable substellar companions, specifically to their masses and effective temperatures.

Because substellar objects continuously cool down as they evolve, it is not possible to determine their mass applying unique relations independent of age, such as the mass–luminosity or mass–effective temperature relations for main-sequence stars. Therefore, in this case one needs to rely on theoretical models providing a grid of luminosities, effective temperatures, and synthetic photometry for different substellar masses as a function of age. In this work, to estimate the minimum masses and temperatures of companions that would have been detected, we used the Ames-COND models (Allard et al. 2001, 2012; Baraffe et al. 2003) for solar metallicity. The COND models are valid up to a $T_{\rm eff}$ of 1300 K and extend down to 100 K. They include the formation of dust in the atmospheres, but dust grains are considered to settle below the photosphere and are not included in the photospheric opacity. To compute the synthetic magnitudes for the Si-2 8.7 μm band we used the PHOENIX Star, Brown Dwarf & Planet Simulator available online[14]. For input we used the transmission file of the Si-2 filter and obtained the isochrones for a set of five different ages: 0.1, 0.5, 1, 5, and 10 Gyr.

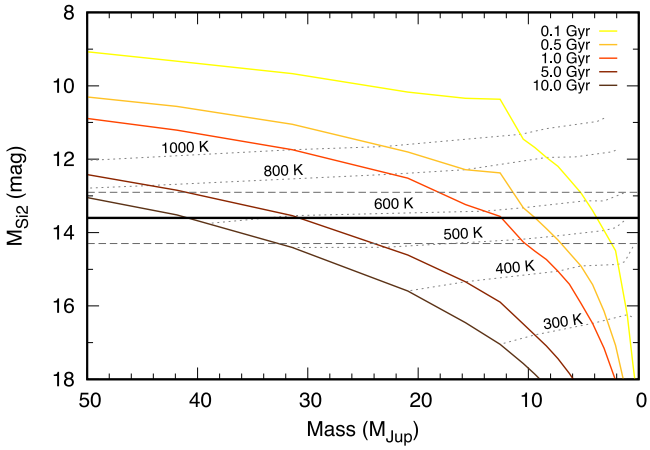

Figure 6. Theoretical absolute magnitudes versus mass of brown dwarfs and giant planets at the Si-2 8.7 μm band obtained using the solar abundance Ames-COND models at ages of 0.1, 0.5, 1, 5, and 10 Gyr. Several corresponding isotherms are plotted with dotted lines. The solid and dashed horizontal lines mark the mean 3σ detection limit range of the survey and a 1σ dispersion: $M_{\rm Si2} = 13.6 \pm 0.7$ mag.

In Figure 6 are plotted the synthetic Si-2 absolute magnitudes versus masses obtained using the COND models, for objects at these five ages, jointly with several isotherms in the $T_{\rm eff}$ range between 300 and 1000 K. The solid and two dashed horizontal lines mark the mean detectability level reached in this program, with the 1σ dispersion taken as the uncertainty: $M_{\rm Si2} = 13.6 \pm 0.7$ mag. For an age of 1 Gyr these limits would extend to objects at the deuterium-burning mass limit and, for 10 Gyr, to about 40 $M_{\rm Jup}$. Assuming an age of 5 Gyr as a typical age expected for stars in the solar vicinity, this sensitivity limit translates to an average minimum mass and temperature of companions that would have been detected

[14] http://phoenix.ens-lyon.fr/simulator/index.faces

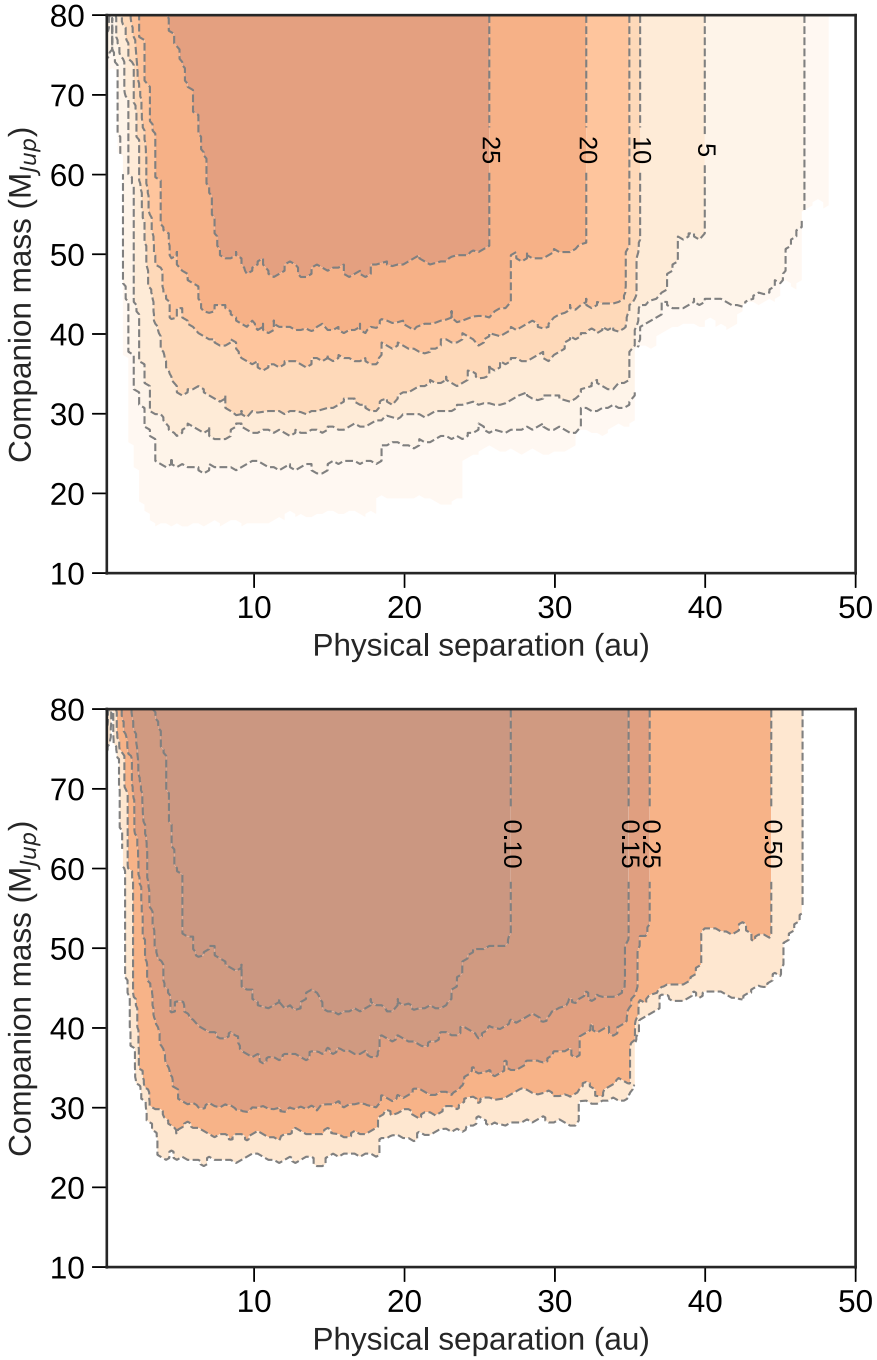

Figure 7. Left panel: overall completeness map of the survey. The contour lines illustrate the number of stars around which the survey is sensitive to substellar companions as a function of companion mass and projected orbital separation. Right panel: upper limit constraints on substellar companions occurrence frequencies, in the same range of masses and projected separations.

of $m = 30 \pm 3\,M_{\rm Jup}$ and $T_{\rm eff} = 600 \pm 40$ K. The derived constraints on companions masses and temperatures around each observed star, assuming a 5 Gyr age, are listed in Table 5.

We converted each detection limit curve into mass limits using the COND evolutionary models and considering the nominal 5 Gyr age, and counted the number of stars for which a companion at a given mass and projected orbital separation would be detectable. The resulting contour map representing the overall depth of our search for the observed sample over a grid of companion masses and separations is presented in Figure 7.

In Table A2, we show the estimations of ages for our sample from the literature and those derived using rotation periods obtained from the literature and the gyrochronology relations from Barnes (2007), Mamajek & Hillenbrand (2008), and Angus et al. (2015). Most of the stars have an estimated age in the range 1–10 Gyr, which justifies the selection of the 5 Gyr isochrone. However, some of them are below the 1 Gyr age and, in these cases, our estimates of detection mass limits were conservative.

We excluded the presence of brown dwarf companions with masses $m \gtrsim 40\,M_{\rm Jup}$ and $T_{\rm eff}$ higher than ~750 K around 24 of the observed stellar systems in the solar vicinity at distances

within 4.6 pc, at the range of angular separations from 1.″0 to 3.″0 depending on the brightness of the target star, and up to 10″. For an average distance of 3.5 pc these angular separations correspond to projected orbital separations in the range from 3.5–10.5 to 35 au. The nondetection of substellar companions throughout this search allowed us to determine an upper limit to the real fraction of companions at the distances and masses mentioned above. We did not assume any shape for the underlying distribution of the population of companions in terms of their masses and semimajor axes, which is equivalent to a uniform, linear, flat distribution. Considering that the number of objects with companions can be well represented by a Poisson distribution, the probability of having no companions is given by the formula:

$$P[k \equiv 0] = \left(e^{-\lambda}\frac{\lambda^k}{k!}\right)_{k\equiv 0} = e^{-\lambda} \quad (1)$$

where λ is the Poisson parameter, k is the number of occurrences, and $\lambda = np$, with n being the number of events (observed stars) and p the real fraction of companions. For a certain confidence level (γ), where $P = 1-\gamma$, the upper limit to the real frequency of substellar companions is $p = -\ln(P)/n$. Considering this general sample of 24 stars, the frequency of such companions is below 9.6% at a confidence level of 90%.

Among these 24 stars, 18 stars are M dwarfs. For them, we were sensitive to substellar companions with $m \gtrsim 40\,M_{\rm Jup}$ and $T_{\rm eff} \gtrsim 750$ K at 1″–10″ separations, which give 1.8–18 au, ∼5–50 au, and 3.5–35 au projected orbital separations for the closest, furthest, and average distances to stars in our sample. Excluding the 10% of the nearest and the furthest observed stars, which set the minimum lower limit and the maximum upper limit of the projected physical separations, we covered from 2.5 to 45 au in 90% of this sample, i.e., our survey is complete from 2.5 to 45 au with a confidence level of 90%. Previous imaging programs that targeted the nearest stars (Oppenheimer et al. 2001; Carson et al. 2011; Dieterich et al. 2012) could already detect companions with such masses. However, they explored wider orbital separations, beyond 10–30 au. The CanariCam survey of nearby M dwarfs allowed us to study for the first time the occurrence of substellar companions with $m > 40\,M_{\rm Jup}$ at orbits below 10 au. With a 90% level of confidence we set an upper limit of 12.8% on their frequency. This value is consistent with constraints derived by other imaging surveys at larger orbital separations, indicating that brown dwarf companions around low-mass M-type stars in the solar vicinity are rare, both at close orbits between 2.5 and 10 au and at wider ones.

For 11 of the observed M dwarfs we were able to detect companions at 1″–10″ separations with $m \gtrsim 30\,M_{\rm Jup}$ and $T_{\rm eff} \gtrsim 600$ K, equivalent to masses and temperatures of the expected T/Y dwarf boundary. We were thus able to establish for the first time a constraint on the upper limit to the frequency of the L- and T-type companions around M dwarfs, at a range of projected orbital separations between 2–3.5 and 35 au. With a 90% confidence level, we found that the frequency of such companions is less than 20% around M stars. Such range of masses and temperatures was explored by imaging surveys so far only in young nearby stars, at wider orbital separations, typically beyond 30–50 au. This imaging search is the first one that probes the presence of L and T companions to M stars at orbital separations around and below 10 au, down to 2.0–3.5 au.

5. Discussion

5.1. Comparison to Other Surveys

We attempt to compare the determined frequency limits of stars harboring substellar companions to results of previous works. Of the numerous programs aiming to detect giant planets and brown dwarf companions, we focus mainly on large, high-contrast imaging surveys including general field surveys probing wide separations and the most recent surveys (see references in Table 6) that placed constraints on substellar companions around M dwarfs. The essential outcomes of many of these programs can be found summarized in, e.g., Table 1 of Chauvin et al. (2015b) and in Bowler (2016) and Vigan et al. (2021). We also consider the results from several RV programs and studies that combine the results from various techniques.

Table 6 summarizes the frequency constraints and the explored intervals of masses and orbital separations or periods, determined by each of these surveys. It is not straightforward to compare the results of these surveys to one another and to our results, because the domains of probed parameter ranges are not the same and different teams make different assumptions regarding the distributions laws of the substellar mass companions. In general, all of the studies agree that the occurrence rates of substellar objects are below 20%, regardless of the companions' mass/separation intervals in question and the masses of the primaries. The majority of surveys point to a maximum frequency of 12% or below, typically of a few percent (∼2%–5%).

As for the low-mass stars, high-contrast imaging searches targeting specifically the M dwarfs, or those including them as part of the target lists, explored objects at young ages of a few tens to a few hundred million years. The most sensitive ones were capable of detecting Jupiter-mass planets at separations down to 10 au, and, most recently, even to 5 au by the SHINE survey (Vigan et al. 2021). On the other side, Doppler measurements restrict the frequencies of planetary companions with minimum masses ($m \sin i$) as small as a few tens of Earth masses and are starting to explore orbital periods of up to 10^4–10^5 days, equivalent to approximately 5–8 au (Fulton et al. 2021; Sabotta et al. 2021).

In this context, our results bridge the explored separation ranges between wide-orbit imaging constraints and those from RVs approaching the snow line. Our limits on the frequency of substellar companions are compatible with previous studies confirming that their presence around M dwarfs is rare. In comparison with recent high-contrast imaging programs, our survey is more sensitive to companions of somewhat higher masses, but at more advanced ages of a few Gyr, and hence of significantly lower $T_{\rm eff}$, extending down to 600 K.

5.2. Stellar Binaries in the Sample

From theory it is expected that a stellar companion alters the formation processes of exoplanets within a protoplanetary disk around the host star (see, e.g., a review by Thebault & Haghighipour 2015). The binary component will also introduce a parameter space of dynamical instability in which we would not expect planets or brown dwarf companions to persist on long timescales (Holman & Wiegert 1999; Haghighipour 2015).

Table 6
Frequencies of Substellar Companions from Imaging and RV Surveys

Survey, Reference	Sample	Occurrence Rate	Masses ($M_{\rm Jup}$)	Separations, Orb. Periods	Conf. Level
SHINE (VLT/SPHERE, Vigan et al. 2021)	subset of 150 stars in young moving groups, typically ∼10–150 Myr	12.6(+12.9, −7.1)% for M dwarfs	1–75	5–300 au	
GPIES (Gemini South/GPI, Nielsen et al. 2019)	300 stars, young (<1 Gyr old), BA and FGK type 0.2–5.0 $M_{\odot}$, (M dwarfs not included)	4.7(+4.4, −2.7)%, 0.8 (+0.8, −0.5)%	5–80, 13–80	10–100 au	95%
VLT/NaCo large program (Vigan et al. 2017)	young nearby stars, mostly <1 Gyr, $d \leqslant 100$ pc, 199 individual stars, FGK types (not M dwarfs) a few stars at >1 Gyr	2.45% (0.25%–5.55%)	5–75	5–500 au	95%
Spitzer/IRAC (Durkan et al. 2016)[a]	73 young stars and 48 exoplanet host stars	<9%	0.5–13	100–1000 au	95%
IDPS survey (Galicher et al. 2016)	292 young nearby stars, median age 120 Myr, 5, 107, 63, 24, 44, 49 B, A, F, G, K, M stars	1.05 (+2.8, −0.7)%, for M dwarfs: <9.15%	0.5–14, 1–13	20–300 au, 10–200 au	95%
Nielsen & Close (2010) analysis	118 stars, majority young stars, only a few at >1 Gyr age	for FGKM stars: <20%, for M stars: <20%	⩾4	22–507, au 9–207 au	95% 68%
GEMINI/NICI campaign, Biller et al. (2013)	80 members of young moving groups, 23 K and 33 M stars	<18% (<6%)[b] <21% (<7%)[b]	1–20	10–150, au 10–50 au	95.4%
SEEDS survey,Uyama et al. (2017)	68 young stellar objects (<10 Myr)	∼2.9%	1–70	50–400 au	
VLT/NaCo L'-band imaging Lannier et al. (2016)	58 young and nearby M dwarfs	4.4(+3.2, −1.3)%	>2	8–400 au	68%
PALMS (Keck/NIRC2, Subaru/HiCIAO, Bowler et al. 2015)	122 nearby (<40 pc) young M dwarfs, 78 single M dwarfs, 90% of stars younger than the Hyades (620 Myr)	<6.0% (<9.9%)[c] 4.5 (+3.1, −2.1)%	5–13, 13–75	10–100, au 10–200 au	
Baron et al. (2019) analysis, AO and seeing-limited imaging combined	344 members of nearby young associations, ∼120 M dwarfs	2.6(+7, −1)%	1–20	20–5000 au	95%
Bowler (2016) analysis	384 unique and single young (∼5–300 Myr) stars, stellar masses between 0.1 and 3.0 $M_{\odot}$	for M stars: <4.2%	5–13	10–100 au	95%
Brandt et al. (2014) analysis	merged samples, 248 unique stars, SpT from late B to mid M, $d \sim$ 5–130 pc	0.52%–4.9%	5–70	10–100 au	95%
TRENDS Montet et al. (2014), RV+imaging survey,	RVs of 111 M dwarfs within 16 pc, imaging follow-up of 4 targets with RV drift	6.5 ± 3.0%	1–13	<20 au	
Clanton & Gaudi (2014, 2016) analysis, RV, microlensing, imaging	synthesis of various samples of M dwarfs	3.8(+1.9, −2.0)%	1–13	1–10^5 days	
HARPS (RV, Bonfils et al. 2013)	102 nearby (<11 pc) M dwarfs	4(+5, −1)%, <1%	∼0.3–3, ∼3–30[d]	10^3–10^4 days, <10^4 days	
AAPS survey (RV, Wittenmyer et al. 2016, 2020)	203 solar type stars (FGK)	6.7(+2, −1)%	0.3–13	∼3–8 au	68.7%
CLS survey (RV, Rosenthal et al. 2021, ApJS25514F)	719 nearby FGKM stars	14.1(+2.0, −1.8)%, 8.9 (+3.0, −2.4)%	⩾0.1[d]	2–8 au, 8–32 au	
CARMENES survey (RV, Sabotta et al. 2021)	subsample of 71 M dwarfs	6(+4, −3)%	⩾0.3[d]	<10^3 days	
This work	18 nearest M dwarfs at $\delta > -25°$	<12.8%, <20%	⩾40, ⩾30	3.5–35 au	90%

Notes.
[a] Re-analysis of archival IRAC data.
[b] Determined applying DUSTY and COND models, respectively.
[c] Assuming a hot-start (cold-start) formation scenario.
[d] Minimum masses, $m \sin i$.

A nonnegligible portion of stars in our targets sample has one or more stellar companions known, including five stellar binaries, two triple systems and two stars with a white dwarf companion. We measure a multiplicity frequency (which quantifies the number of multiple systems within our sample) and a companion frequency (which quantifies the total number of companions) of $36 \pm 14\%$ and $44 \pm 16\%$, respectively, which are consistent within wide uncertainties with the comprehensive determinations by Reylé et al. (2021) in the 10 pc sample and by Ballantyne et al. (2021) for the M dwarfs. For the statistical analysis, we considered the relatively close systems ($s \lesssim 50$ au; Sirius, GJ 65, GJ 866, Procyon, GJ 860, and GJ 1245) as individual systems and those having components at wider average orbital separations ($s \gtrsim 50$ au; GJ 820AB, GJ 725AB, and GJ 15AB) as two individual stars.

We add a note of caution that such an approach introduces a potential physical bias in the interpretation of our analysis. Our search probes both circumstellar and circumbinary companions depending on the separation of the binaries, which are very different science cases to one another and to a search around single stars only. We recorded a null companion detection in these systems. However, any secondary component introduces a region of instability at a certain range of physical separations for both S- and P-type orbits (Holman & Wiegert 1999; Desidera & Barbieri 2007), in which we would not expect an additional body to be found. Thus, an element of bias is inherent in the statistical result derived from a combined single and binary star sample.

Several works have concluded that binarity has a minimal effect on overall planet frequency (Bonavita & Desidera 2007; Bergfors et al. 2013; Piskorz et al. 2015; Southworth et al. 2020). By contrast, some recent observational studies demonstrate an excess of wide stellar companions to stars that host high-mass hot Jupiters and brown dwarf companions on short-period orbits (Ngo et al. 2016; Fontanive et al. 2019; Fontanive & Bardalez Gagliuffi 2021; Moe & Kratter 2021). These conclude that certain types of binaries may support the process of formation of close-in high-mass planetary and substellar companions. Although early research on this front has been carried out, e.g., by the SPOTS (Bonavita et al. 2016; Asensio-Torres et al. 2018) and the VIBES (Hagelberg et al. 2020) surveys, a more detailed analysis of the effect multiplicity has on the occurrence of substellar companions in general requires a larger, dedicated sample that is complete in both single stars and binaries.

5.3. Known Planets Hosts

As many as 12 of the 33 stars in the sample have at least one small planet of a few to a few tens of Earth masses on a close orbit at around 1 au or less. All of these cases, except the G8.5V-type τ Cet, are M-dwarf stars. By contrast, only two of these stars were found to host more massive planets—K2.0V ϵ Eri (b: $m \sin i = 0.78\, M_{\rm Jup}$ at 3.48 ± 0.02 au) and M3.5V GJ 876 (b: $m \sin i = 2.27\, M_{\rm Jup}$ at $a = 0.21$ au; c: $m \sin i = 0.71\, M_{\rm Jup}$ at $a = 0.13$ au). This is in line with results of surveys that noticed initial indications that frequencies of more massive giant planets scale positively with the host star mass (e.g., Johnson et al. 2010; Bowler 2016).

There are no theoretical premises indicating that such close-in planets will preclude the formation of more massive companions in wider orbits. Instead, observational studies showed that hot Jupiter host stars tend to have far-away companions (e.g., Knutson et al. 2014; Lodieu et al. 2014; Wang et al. 2015). The dynamical interactions between multiple planets or a distant brown dwarf companion may affect the final orbital configuration of the system. A variety of mechanisms, such as planet–planet scattering, the Kozai–Lidov effect, or secular gravitational interactions (Hansen & Murray 2015; Naoz 2016), have been invoked for smaller planets to explain inwards migration to short orbital periods (Masset & Papaloizou 2003).

6. Conclusions and Final Remarks

We completed a deep, high spatial resolution imaging search of substellar companions around the nearest northern stars in the mid-IR at 8.7 μm using the CanariCam instrument on the 10.4 m GTC telescope. Our target sample included 25 stellar systems composed of 33 individual stars, with declinations $\delta > -25°$ within 5 pc of the Sun. No previously undetected companions were identified in our survey.

We explored the angular separations between 1″–3″ and 10″ with sensitivities sufficient to detect companions with masses and temperatures higher than $40\, M_{\rm Jup}$ and 750 K for 24 of the observed stars, and as low as $30\, M_{\rm Jup}$ and 600 K for 11 M-type stars. Considering an average distance of 3.5 pc of our sample, 3.5–35 au projected orbital separations were probed for faint companions. The nondetections enabled us to determine upper limits for the fraction of substellar companions. At a 90% confidence level, we found that fewer than 9.6% of the nearby stars have companions with $m \gtrsim 40\, M_{\rm Jup}$ and $T_{\rm eff} \gtrsim 750$ K, and that fewer than 20% of the closest M dwarfs have L and T companions with $m > 30\, M_{\rm Jup}$ and $T_{\rm eff} \gtrsim 600$ K within the range of explored physical separations. This is one the first imaging programs capable of detecting mature substellar companions in this range of masses and temperatures below 10 au separations and provides evidence that substellar companions to low-mass M dwarfs are rare also at such closer orbits. Concurrently, extending the constraints beyond 5 au, our results are complementary to the evidence brought by RV programs (e.g., Bonfils et al. 2013; Winn & Fabrycky 2015; Morales et al. 2019; Sabotta et al. 2021), which find the occurrence of giant planets around M stars to be less than 3% at orbital periods up to 25–30 yr (~5 au).

This work demonstrates that the modern ground-based mid-IR imaging instruments operating on 10 m class telescopes can reach angular resolutions and sensitivity limits as good as and, in certain cases (e.g., nearby, relatively old stars), better than adaptive optics systems in the optical or near-IR or space telescopes. This technique presents a great potential for direct imaging detection and studies of brown dwarfs and exoplanets. Our survey was not extensive enough to determine more precisely the true fraction of L and T brown dwarf companions at close orbits. Nonetheless results on the observed sample provide valuable constraints for next-generation facilities, such as the James Webb Space Telescope or the Extremely Large Telescope, which will allow for detection and accurate characterization of the coldest companions to stars (Quanz et al. 2015; Danielski et al. 2018).

We thank the anonymous referee for a careful review of our manuscript and his/her constructive comments that substantially helped improve the quality of the paper. We are grateful to the GTC staff for performing the CanariCam observations.

Based on observations made with the Gran Telescopio Canarias (GTC), installed at the Spanish Observatorio del Roque de los Muchachos of the Instituto de Astrofísica de Canarias, in the island of La Palma. B.G. and D.J.P. acknowledge support from the UK Science and Technology Facilities Council (STFC) via the Consolidated Grant ST/R000905/1. V.J.S.B., M.R.Z.O., and J.A.C. acknowledge financial support from the Agencia Estatal de Investigación of the Ministerio de Ciencia, Innovación y Universidades and the European Regional Development Fund through projects PID2019-109522GB-C5 [1, 3]. We acknowledge the use of Carmencita, the CARMENES input catalog (Caballero et al. 2016). This research has made use of the SIMBAD database, operated at CDS, Strasbourg, France.

Appendix A
Known Planetary/substellar Companions of the Sample Stars

In Table A1 we include our notes with the essential information regarding the currently known exoplanets and substellar companions of the sample stars gathered through a literature search. Table A2 incorporates available age estimations of the observed stars and the corresponding references.

Table A1
Notes on the Currently Known Exoplanets and Substellar Companions of the Sample Stars

Star		Notes
GJ 699	Barnard's Star	Ribas et al. 2018: RV super-Earth planet near the snow line; from CARMENES, HARPS, HARPS-N 20 yr monitoring; $m \sin i = 3.23 \pm 0.44\ M_{\oplus}$, $a = 0.404 \pm 0.018$ au, $P_{\rm orb} = 232.8$ d, $\rho = 221 \pm 10$ mas; evidence for a second, longer period signal at ∼6600 d, the presence of an outer planet cannot be ruled out. The fit would suggest an object of $\gtrsim 15\ M_{\oplus}$ on a ∼4 au orbit.
GJ 406	CN Leo	Monitored with HARPS (Bonfils et al. 2013), HIRES (Butler et al. 2017), and CARMENES (Alonso-Floriano et al. 2015). Relatively active flare star (Reiners et al. 2007). No planets reported yet.
GJ 411	Lalande 21185	One RV planet, confirmed status. Discovered by Díaz et al. (2019), confirmed by Stock et al. (2020a) using HIRES, SOPHIE, and CARMENES data; $m \sin i = 2.69 \pm 0.25\ M_{\oplus}$, 0.0789 ± 0.0007au, $P_{\rm orb} = 12.946 \pm 0.005$ d
GJ 244	Sirius	HST astrometry rules out companions larger than a small brown dwarf or large exoplanet (Bond et al. 2017);: $m > 0.033\ M_{\odot}$ orbiting in 0.5 yr, and $m > 0.014\ M_{\odot}$ in 2 yr. No planets reported yet.
GJ 65 AB	BL Cet + UV Cet	M5.5V + M6V binary at $a = 2.1$–8.8 au, $P_{\rm orb} = 26.52$ yr, $e = 0.62$; No planets reported yet.
GJ 729	V1216 Sgr	Monitored with HARPS (Bonfils et al. 2013); on the CARMENES GTO target list (Reiners et al. 2018). No planets reported yet.
GJ 905	HH And	SPIRou Input Catalog (Fouqué et al. 2018) − a slow rotator star $P_{\rm rot} = 99.58$ d, rejected as a spectroscopic binary candidate. On the CARMENES GTO target list (Reiners et al. 2018). No planets reported yet.
GJ 144	ϵ Eridani	One confirmed planet (ϵ Eri b) plus one unconfirmed candidate planet (ϵ Eri c) ϵ Eri b: 0.78 $M_{\rm Jup}$, 3.48 ± 0.02 au, $P_{\rm orb}$ 7.37 ± 0.07 yr (Mawet et al. 2019), using Ms band (4.7 μm) Keck/NIRC2 imaging and RV data (HIRES, HARPS, others) over 30 yr. Direct imaging constraints for 200, 400, and 800 Myr age: 3.0, 4.5, 6.5 $M_{\rm Jup}$ at 1 au; 1.5, 1.7, 2.5 $M_{\rm Jup}$ at 2 au; 0.8, 1.7, 5.0 $M_{\rm Jup}$ at 3 au. The putative planet "c" should be orbiting at around 40 au, to shape the dust disk. Limits from Spitzer imaging (Janson et al. 2015): $m = 0.5$–$2.5\ M_{\rm Jup}$ at 20–140 au separations (at 800 Myr).
GJ 447	FI Vir	An exo-Earth planet discovered in HARPS RVs (Bonfils et al. 2018), $m \sin i = 1.35 \pm 0.2\ M_{\oplus}$, $a = 0.049 \pm 0.002$ au, $P_{\rm orb} = 9.86 \pm 0.01$ d. CARMENES GTO target star (Reiners et al. 2018).
GJ 866 ABC	EZ Aqr	A compact triple system of M dwarfs (Delfosse et al. 1999; Woitas et al. 2000) AC—spectroscopic binary 0.012–0.016 au, $\rho \sim 0.01''$, $P_{\rm orb} \sim 3.8$ d; AC-B—0.41–0.77 au, $\rho \sim 0.36''$, $P_{\rm orb} = 823$ d. Well-determined dynamical masses: A 0.1216, B 0.1161, C 0.0957 $M_{\odot}$. No planets reported yet.
GJ 820 A	61 Cyg A	Limits from RVs: 0.09–0.98 $M_{\rm Jup}$ between 0.05–5.2 au, by Wittenmyer et al. (2006). No planets reported yet.
GJ 820 B	61 Cyg B	Possibly a third body orbiting the B component, from proper-motion anomalies in Gaia DR2 (Kervella et al. 2019); hypothetically, a companion of $m = 2.95$ [$M_{\rm Jup}$ au $^{(-1/2)}$] normalized to $r = 1$ au orbit explains the anomaly. Limits from RVs: 0.07–0.8 $M_{\rm Jup}$ between 0.05–5.2 au, from Wittenmyer et al. (2006). No planets reported yet.
GJ 280	Procyon	White dwarf (DQZ) companion Procyon B, $P_{\rm orb} = 40.8$ yr, $e = 0.4$, average $a = 15$ au (8.9–21.0 au); Bond et al. (2015). HST astrometry excludes $m \gtrsim 10\ M_{\rm Jup}$ companions at >1.5 yr orbital periods (Bond et al. 2015). No planets reported yet.
GJ 725 A	HD 173739	Monitored using HARPS-N (Berdiñas et al. 2016). On the CARMENES GTO target list (Reiners et al. 2018). No planets reported yet.
GJ 725 B	HD 173740	A candidate planet proposed by Berdiñas et al. (2016) from HARPS-N RV: $m \sin i = 1.2\ M_{\oplus}$, $P_{\rm orb} = 2.7 \pm 0.3$ d, $a = 0.025$ au (S-type orbit). CARMENES GTO target star (Reiners et al. 2018).
GJ 15 A	GX And	Two planets detected: b: $m \sin i = 3.03 \pm 0.4\ M_{\oplus}$, 0.07 au, $P_{\rm orb} = 11.4$ d, (HIRES, Howard et al. 2014); c: $m \sin i = 36$ $(+25, -18) M_{\oplus}$, 5.4 au, $P_{\rm orb}$ ∼7600 d, longest period Neptune-mass exoplanet (CARMENES, Trifonov et al. 2018), both planets confirmed with more data: HIRES, CARMENES, HARPS-N (Pinamonti et al. 2018)
GJ 15 B	GQ And	On the CARMENES GTO target list (Reiners et al. 2018). No planets reported yet.
GJ 1111	DX Cnc	On the CARMENES target list. No planets reported yet.
GJ 71	τ Ceti	A four-planet system found using >9000 HARPS and HIRES RV measurements from 2003 to 2013 (Tuomi et al. 2013; Feng et al. 2017): g: $m \sin i = 1.75$ [+0.25, −0.40] $M_{\oplus}$, $a = 0.13$ au, $P_{\rm orb} = 20.0$ d; h: $m \sin i = 1.83$ [+0.68, −0.26] $M_{\oplus}$, $a = 0.24$ au, $P_{\rm orb} = 49.4$ d; e: $m \sin i = 3.93$ [+0.86, −0.64] $M_{\oplus}$, $a = 0.54$ au, $P_{\rm orb} = 162.9$ d; f: $m \sin i = 3.93$ [+1.05, −1.37] $M_{\oplus}$, $a = 1.33$ au, $P_{\rm orb} = 636.1$ d. Planets originally denoted b, c, d were not confirmed. All four planets tightly packed in orbits <1.5 au. Tangential velocity anomaly indicates a possible presence of a Jupiter-analog planet, by at most 5 $M_{\rm Jup}$ if orbiting between 3 and 20 au (Kervella et al. 2019).
GJ 54.1	YZ Cet	A three-planet system in compact orbits confirmed (HARPS RVs, Astudillo-Defru et al. 2017a). Small, Earth-mass planets: $P_{\rm orb} = 1.97$, 3.06, 4.66 d; $m \sin i = 0.75 \pm 0.13$, 0.98 ± 0.14, and $1.14 \pm 0.17\ M_{\oplus}$. Fourth planet candidate discarded by Stock et al. (2020b).
GJ 273	Luyten's Star	Two planets detected using ∼13 yr HARPS RV monitoring (Astudillo-Defru et al. 2017b): c: $m \sin i = 1.18 \pm 0.16\ M_{\eth}$, $a = 0.0365$au, $P_{\rm orb} = 4.7234 \pm 0.0004$d; b: $m \sin i = 2.89 \pm 0.26\ M_{\eth}$, $a = 0.09110 \pm 0.00002$au, $P_{\rm orb} = 18.65 \pm 0.01$ d. GJ 273b is a super-Earth within the habitable zone (Kopparapu et al. 2016). On the CARMENES GTO target list (Reiners et al. 2018).
SO 0253+1652	Teegarden's Star	Two Earth-mass planets discovered with CARMENES (Zechmeister et al. 2019): b: $m \sin i = 1.05\ M_{\eth}$, $a = 0.025$ au, $P_{\rm orb} = 4.91$ d; c: $m \sin i = 1.11\ M_{\eth}$, $a = 0.044$ au, $P_{\rm orb} = 11.41$ d.

Table A1
(Continued)

Star		Notes
GJ 860 AB	Kruger 60 AB	M3V + M4V binary (a = 5.5–13.5 au, $P_{\rm orb}$ = 44.6 yr, e = 0.41, nearly face-on orbit i = 167.2°; Knapp & Nanson 2018). Astrometric observations rule out companions $\geqslant$0.45 and $\geqslant$0.37 $M_{\rm Jup}$ at $\geqslant$1 au orbits around A and B components, respectively (Hełminiak et al. 2009). RVs monitored with HIRES (Butler et al. 2017). No planets reported yet.
GJ 83.1	TZ Ari	Two RV planets in a 3:1 mean motion resonance (Feng et al. 2020) using HARPS and HIRES data: b: $m \sin i$ = 12.8–42.8 $M_{\oplus}$, a = 0.40 au, $P_{\rm orb}$ = 243.1 d; c: $m \sin i$ = 96.0–174 $M_{\oplus}$, a = 0.87 au, $P_{\rm orb}$ = 773.4 d. On the CARMENES GTO target list (Reiners et al. 2018).
GJ 687	LHS 450	Two RV planets reported (Burt et al. 2014; Feng et al. 2020): b: $m \sin i$ = 18.4 $M_{\oplus}$, a = 0.16 au, $P_{\rm orb}$ = 38.1 d; c: $m \sin i$ = 16.0 $M_{\oplus}$, a = 1.16 au, $P_{\rm orb}$ = 692–796 d, e = 0.4. On the CARMENES GTO target list (Reiners et al. 2018).
GJ 1245 ABC	LHS 3494	Triple system composed of M dwarfs: M5 + M5 + M8 (AC-B: 33 au, A-C: 8 au; McCarthy et al. 1988; Hawley et al. 2014), Kepler light curves of A and B analyzed, $P_{\rm rot}$=0.26 and 0.71 d for A and B, respectively (Lurie et al. 2015). HIRES and HPF RV planet search (Robertson et al. 2020). No planets reported yet.
GJ 876	IL Aqr	A four-planet system currently known (RVs), first two planets discovered in 1998 and 2001 (Marcy et al. 1998, 2001): d: $m \sin i$ = 6.83 $M_{\oplus}$, a = 0.021 au, $P_{\rm orb}$ = 1.94 d; c: $m \sin i$ = 0.714 $M_{\rm Jup}$, a = 0.129 au, $P_{\rm orb}$ = 30.01 d; b: $m \sin i$ = 2.275 $M_{\rm Jup}$, a = 0.208 au, $P_{\rm orb}$ = 61.12 d; e: $m \sin i$ = 14.6 $M_{\oplus}$, a = 0.334 au, $P_{\rm orb}$ = 124.26 d. Mean motion resonance 1:2:4 of the outermost planets. A triple conjunction of the outer three planets once per every orbit of the outer planet,"e" (Rivera et al. 2010; Millholland et al. 2018). GJ 876 is a candidate parent system for the 1I/'Oumuamua object (Dybczyński & Królikowska 2018).
GJ 1002	LHS 2	Surveyed by HARPS and CARMENES (Bonfils et al. 2013; Reiners et al. 2018). No planets reported yet.

Table A2
Ages of the Stars in the Sample

Star	Age Lit. (Gyr)	Ref.	P_{rot} (d)	Ref.	Age (Gyr)
GJ 699	7–10	Rib18	148.6 ± 0.1	SM15	>10
GJ 406	0.1–1	Pav06	2.704 ± 0.003	DA19	0.01–0.08
GJ 411	5–10	…	48.0	KS07	2–10
GJ 244	0.228 ± 0.010	Bond17	…	…	…
GJ 65 AB	5.0	MacD18	0.243 ± 0.0005	Bar17	…
GJ 729[a]	<1.0	War08	2.8502	CC21	0.01–0.08
GJ 905	…	…	106.0 ± 6.0	DA19	>10
GJ 144	0.4–0.8	Jan15	11.1 ± 0.03	GB95	0.3–3.2
GJ 447	9.45 ± 0.60	Man15	163 ± 3	DA19	>10
GJ 866 (AC)	…	…	…	…	…
GJ 820 A	6.1 ± 1	Ker08	35.37 ± 10	Don96	1–10
GJ 820 B	6.1 ± 1	Ker08	37.84 ± 10	Don96	1–10
GJ 280	1.87 ± 0.13	Lie13	23 ± 2	Ayr91	…
GJ 725 A	3.0	Man15	…	…	…
GJ 725 B	2.4	Man15	…	…	…
GJ 15A	3.02	Man15	45 ± 4.4	SM18	1–10
GJ 15B	2.754	Man15	…	…	…
GJ 1111[a]	0.2–0.4	Les06	0.459 ± 0.00001	DA19	…
GJ 71	5.8	Mam08	34	Bal96	3.5–10
GJ 54.1	5.0	…	69.2 ± 2.4	DA19	>10
GJ 273	>8.0	Poz20	93.5 ± 16	SM17	>10
SO 0253+1652	>8.0	Zech19	∼100	Zech19	>10
GJ 860 AB	…	…	…	…	…
GJ 83.1	∼5	Yee17	…	…	…
GJ 687	…	…	∼60	Bur14	1.5–10
GJ 1245 AC	…	…	0.2632 ± 0.0001	Haw14	…
GJ 1245 B	∼0.3	…	0.709 ± 0.001	Haw14	…
GJ 876[b]	0.1–5	Cor10	81.0 ± 0.8	DA19	>10
GJ 1002	…	…	…	…	…

Note.
[a] Castor YMG member.
[b] Slow rotator.
REFERENCES: Rib18: Ribas et al. (2018), SM15: Suárez Mascareño et al. (2015), DA19: Díez Alonso et al. (2019), Pav06: Pavlenko et al. (2006), KS07: Kiraga & Stepien (2007), Bond17: Bond et al. (2017), MacD18: MacDonald et al. (2018), Bar17: Barnes et al. (2017), War18: Wargelin et al. (2008), CC21: Cortes-Contreras et al. 2021 in prep, Jan15: Janson et al. (2015), GB15: Gray & Baliunas (1995), Man15: Mann et al. (2015), Ker08: Kervella et al. (2008), Don96: Donahue et al. (1996), Lie13: Liebert et al. (2005), Ayr91: Ayres (1991), SM18: Suárez Mascareño et al. (2018), Les06: Lestrade et al. (2006), Mam08: Mamajek & Hillenbrand (2008), Bal96: Gray & Baliunas (1995), Poz20: Pozuelos et al. (2020), SM17: Suárez Mascareño et al. (2017), Zech19: Zechmeister et al. (2019), Yee17: Yee et al. (2017), Bur14: Burt et al. (2014), Cor10: Correia et al. (2010).

Appendix B
A Full Set of the Final CanariCam Images

Figures B1 and B2 contain a collection of the processed CanariCam images of all of the observed stars. Figure B1 contains a set of common size ($25\farcs6 \times 19\farcs2$) central parts of the images, whereas Figure B2 includes full FOV mosaics. All of the reduced image stacks can be retrieved from https://cloud.iac.es/index.php/s/kT3cCdP9Wxw92gZ.

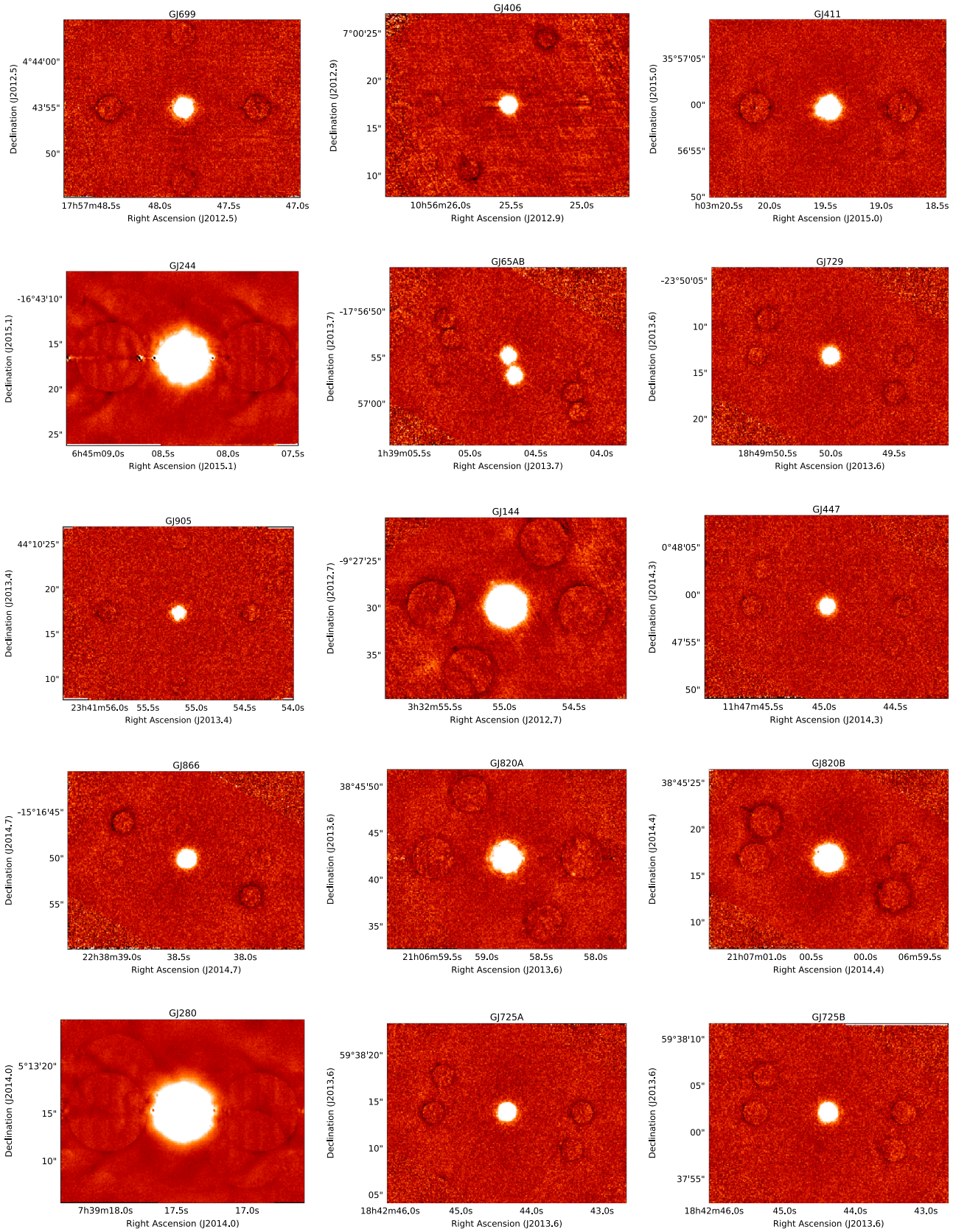

Figure B1. The final, deepest CanariCam Si-2 filter (8.7 μm) images of the observed stars of the 5 pc sample. Counts are in linear scale and in the $\pm 7\sigma$ range relative to the zero background. Shown field of view is $25\farcs6 \times 19\farcs2$, orientation is North up and East to the left. The coordinates correspond to the first observing epoch, taking into account the proper motion.

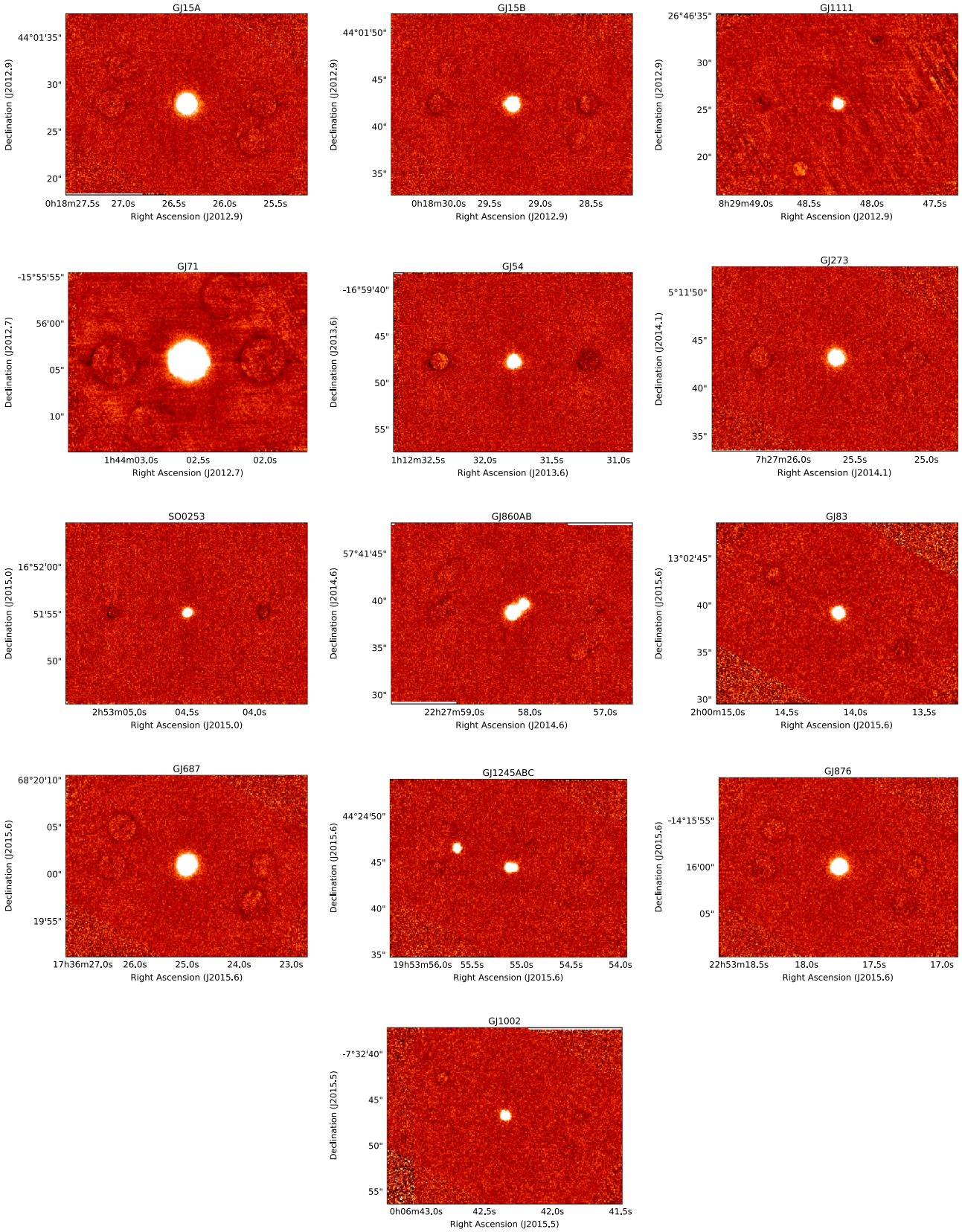

Figure B1. (Continued.)

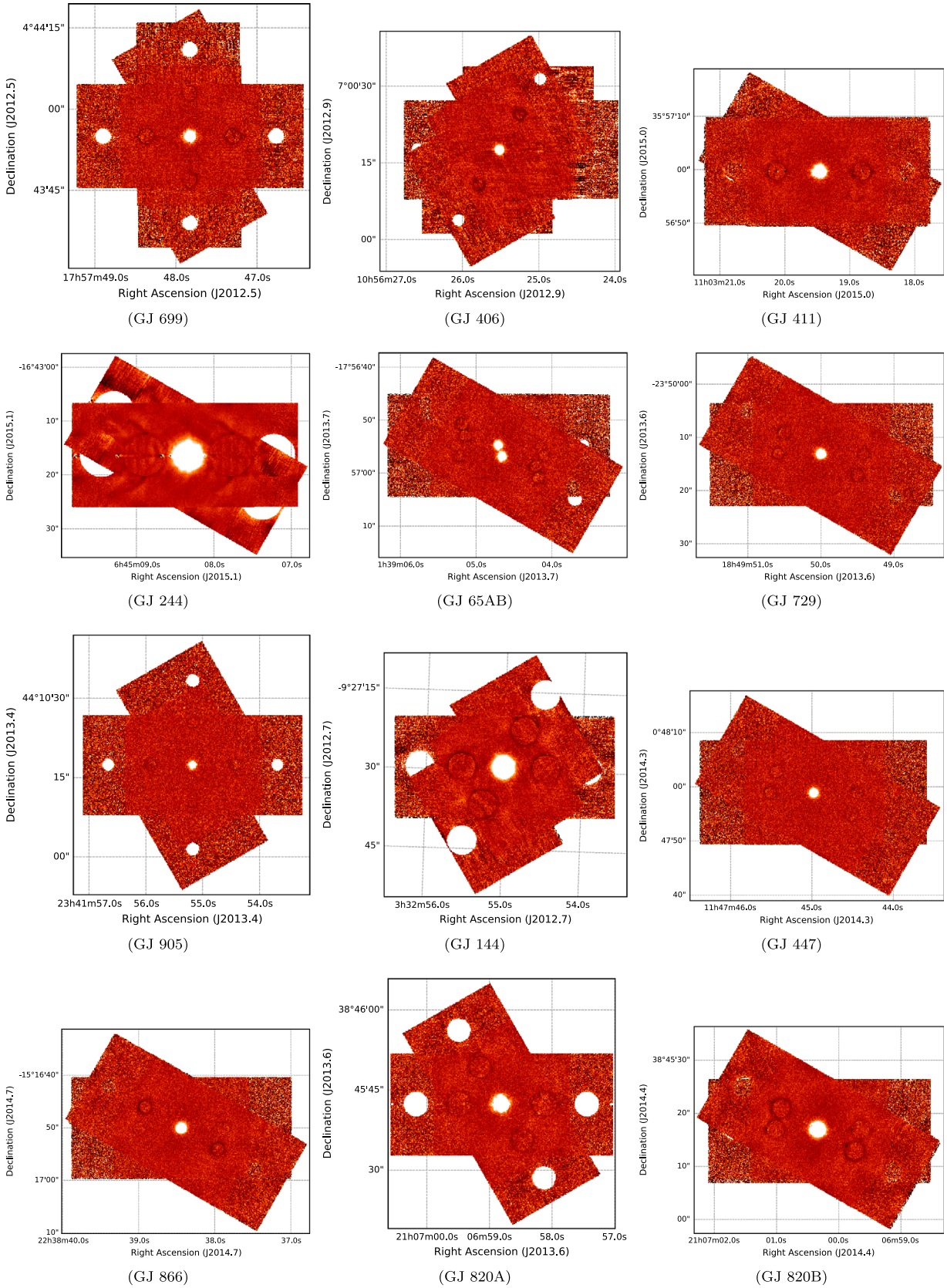

Figure B2. Same as Figure B1 but for full field of view mosaics. The .tar.gz package contains 28 FITS images of the sources shown in this figure.

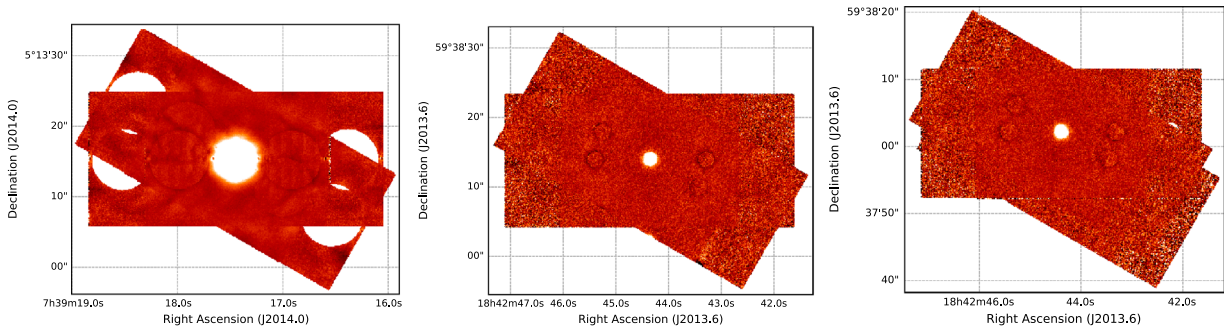

(GJ 280) (GJ 725A) (GJ 725B)

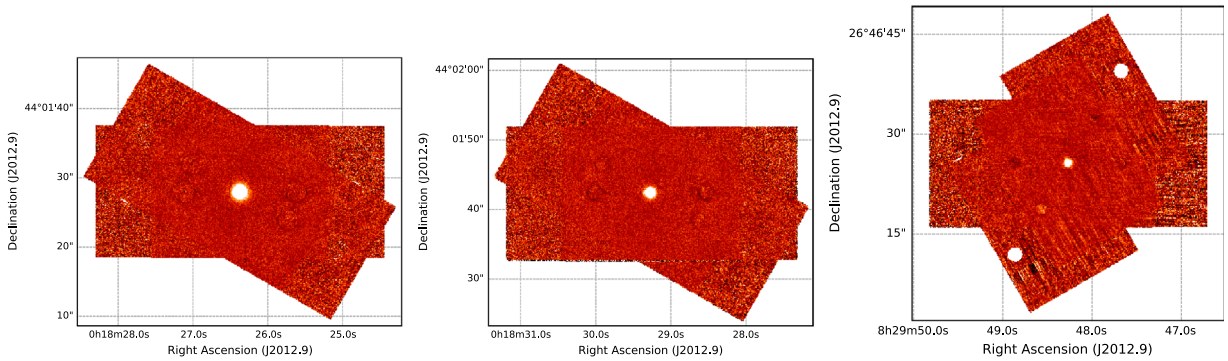

(GJ 15A) (GJ 15B) (GJ 1111)

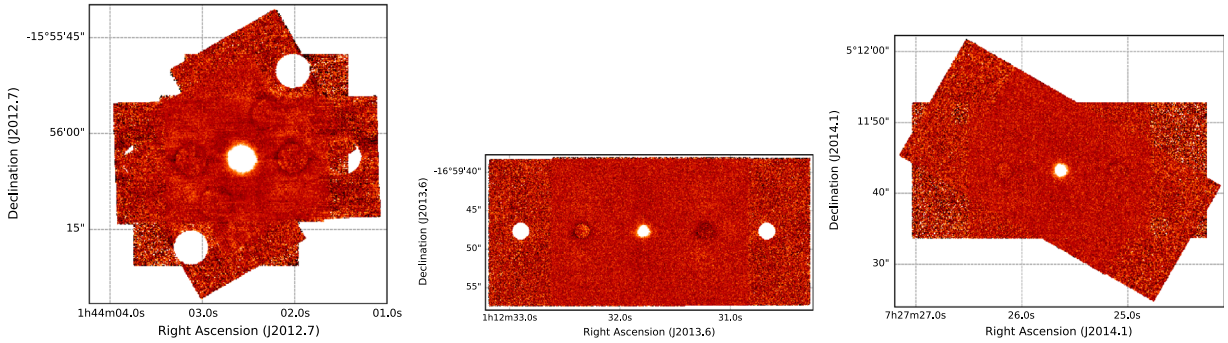

(GJ 71) (GJ 54.1) (GJ 273)

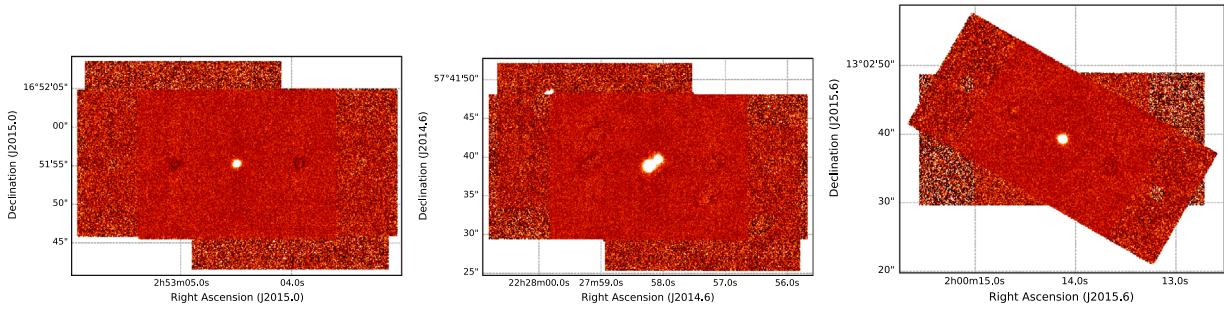

(S0 0253+1652) (GJ 860AB) (GJ 83.1)

Figure B2. (Continued.)

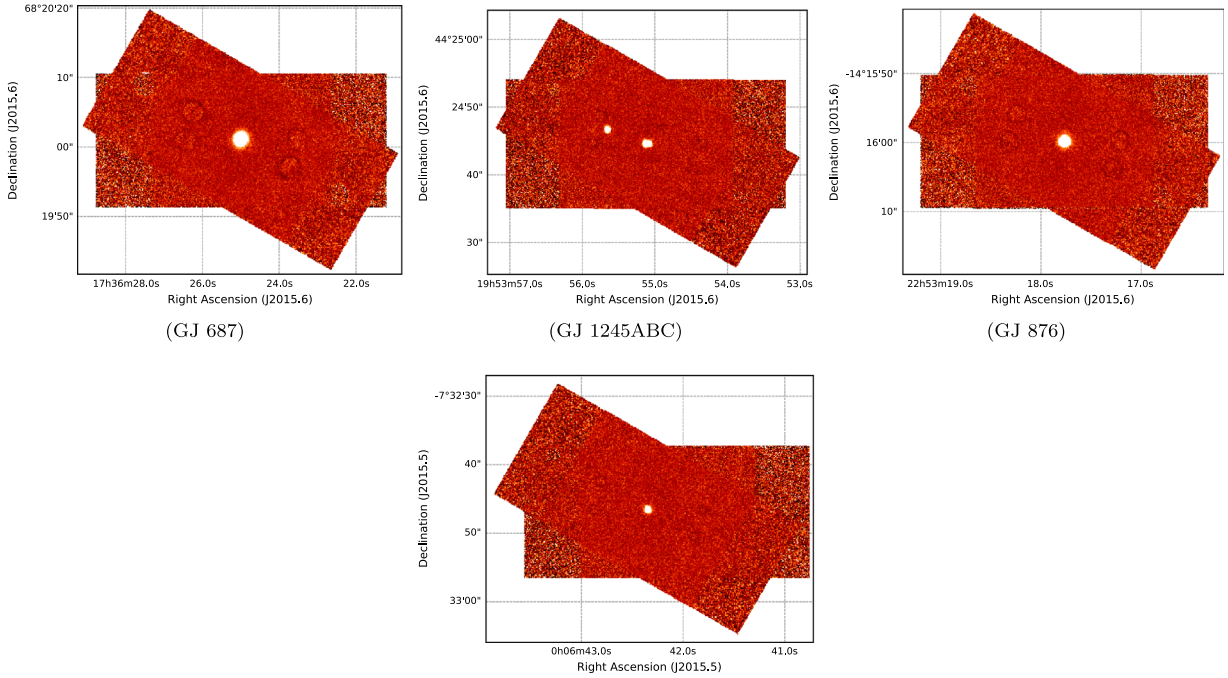

Figure B2. (Continued.)

ORCID iDs

Bartosz Gauza https://orcid.org/0000-0001-5452-2056
Víctor J. S. Béjar https://orcid.org/0000-0002-5086-4232
Rafael Rebolo https://orcid.org/0000-0003-3767-7085
María Rosa Zapatero Osorio https://orcid.org/0000-0001-5664-2852
José A. Caballero https://orcid.org/0000-0002-7349-1387
David J. Pinfield https://orcid.org/0000-0002-7804-4260
Christopher Packham https://orcid.org/0000-0001-7827-5758

References

Allard, F., Hauschildt, P. H., Alexander, D. R., Tamanai, A., & Schweitzer, A. 2001, ApJ, 556, 357
Allard, F., Homeier, D., Freytag, B., & Sharp, C. M. 2012, in EAS Publ. Ser. 57, Low-Mass Stars and the Transition Stars/Brown Dwarfs - EES2011, ed. C. Reylé, C. Charbonnel, & M. Schultheis (Les Ulis: EDP Sciences), 3
Alonso-Floriano, F. J., Morales, J. C., Caballero, J. A., et al. 2015, A&A, 577, A128
Angus, R., Aigrain, S., Foreman-Mackey, D., & McQuillan, A. 2015, MNRAS, 450, 1787
Asensio-Torres, R., Janson, M., Bonavita, M., et al. 2018, A&A, 619, A43
Astudillo-Defru, N., Díaz, R. F., Bonfils, X., et al. 2017a, A&A, 605, L11
Astudillo-Defru, N., Forveille, T., Bonfils, X., et al. 2017b, A&A, 602, A88
Ayres, T. R. 1991, ApJ, 375, 704
Ballantyne, H. A., Espaas, T., Norgrove, B. Z., et al. 2021, MNRAS, 507, 4507
Baraffe, I., Chabrier, G., Barman, T. S., Allard, F., & Hauschildt, P. H. 2003, A&A, 402, 701
Barnes, J. R., Jeffers, S. V., Haswell, C. A., et al. 2017, MNRAS, 471, 811
Barnes, S. A. 2007, ApJ, 669, 1167
Baron, F., Lafrenière, D., Artigau, É., et al. 2019, AJ, 158, 187
Berdiñas, Z. M., Amado, P. J., Anglada-Escudé, G., Rodríguez-López, C., & Barnes, J. 2016, MNRAS, 459, 3551
Bergfors, C., Brandner, W., Daemgen, S., et al. 2013, MNRAS, 428, 182
Biller, B. A., Liu, M. C., Wahhaj, Z., et al. 2013, ApJ, 777, 160
Bonavita, M., & Desidera, S. 2007, A&A, 468, 721
Bonavita, M., Desidera, S., Thalmann, C., et al. 2016, A&A, 593, A38
Bond, H. E., Gilliland, R. L., Schaefer, G. H., et al. 2015, ApJ, 813, 106
Bond, H. E., Schaefer, G. H., Gilliland, R. L., et al. 2017, ApJ, 840, 70
Bonfils, X., Delfosse, X., Udry, S., et al. 2013, A&A, 549, A109
Bonfils, X., Astudillo-Defru, N., Díaz, R., et al. 2018, A&A, 613, A25
Bonnefoy, M., Zurlo, A., Baudino, J. L., et al. 2016, A&A, 587, A58
Bonnefoy, M., Perraut, K., Lagrange, A. M., et al. 2018, A&A, 618, A63
Bowler, B. P. 2016, PASP, 128, 102001
Bowler, B. P., Liu, M. C., Shkolnik, E. L., & Tamura, M. 2015, ApJS, 216, 7
Brandt, T. D., McElwain, M. W., Turner, E. L., et al. 2014, ApJ, 794, 159
Burt, J., Vogt, S. S., Butler, R. P., et al. 2014, ApJ, 789, 114
Butler, R. P., Vogt, S. S., Laughlin, G., et al. 2017, AJ, 153, 208
Caballero, J. A., Cortés-Contreras, M., Alonso-Floriano, F. J., et al. 2016, in 19th Cambridge Workshop on Cool Stars, Stellar Systems, and the Sun (CS19), 148
Carson, J. C., Marengo, M., Patten, B. M., et al. 2011, ApJ, 743, 141
Chauvin, G., Vigan, A., Bonnefoy, M., et al. 2015a, A&A, 573, A127
Chauvin, G., Vigan, A., Bonnefoy, M., et al. 2015b, A&A, 573, A127
Chinchilla, P., Béjar, V. J. S., Lodieu, N., Zapatero Osorio, M. R., & Gauza, B. 2021, A&A, 645, A17
Clanton, C., & Gaudi, B. S. 2014, ApJ, 791, 91
Clanton, C., & Gaudi, B. S. 2016, ApJ, 819, 125
Cohen, M., Wheaton, W. A., & Megeath, S. T. 2003, AJ, 126, 1090
Correia, A. C. M., Couetdic, J., Laskar, J., et al. 2010, A&A, 511, A21
Danielski, C., Baudino, J.-L., Lagage, P.-O., et al. 2018, AJ, 156, 276
Delfosse, X., Forveille, T., Udry, S., et al. 1999, A&A, 350, L39
Desidera, S., & Barbieri, M. 2007, A&A, 462, 345
Díaz, R. F., Delfosse, X., Hobson, M. J., et al. 2019, A&A, 625, A17
Dieterich, S. B., Henry, T. J., Golimowski, D. A., Krist, J. E., & Tanner, A. M. 2012, AJ, 144, 64
Díez Alonso, E., Caballero, J. A., Montes, D., et al. 2019, A&A, 621, A126
Donahue, R. A., Saar, S. H., & Baliunas, S. L. 1996, ApJ, 466, 384
Durkan, S., Janson, M., & Carson, J. C. 2016, ApJ, 824, 58
Dybczyński, P. A., & Królikowska, M. 2018, A&A, 610, L11
Feng, F., Tuomi, M., Jones, H. R. A., et al. 2017, AJ, 154, 135
Feng, F., Shectman, S. A., Clement, M. S., et al. 2020, ApJS, 250, 29
Fontanive, C., & Bardalez Gagliuffi, D. 2021, FrASS, 8, 16
Fontanive, C., Rice, K., Bonavita, M., et al. 2019, MNRAS, 485, 4967
Fouqué, P., Moutou, C., Malo, L., et al. 2018, MNRAS, 475, 1960
Fulton, B. J., Rosenthal, L. J., Hirsch, L. A., et al. 2021, ApJS, 255, 14
Gaia Collaboration 2018, A&A, 616, A1
Gaia Collaboration 2021, A&A, 649, A1
Galicher, R., Marois, C., Macintosh, B., et al. 2016, A&A, 594, A63
Gauza, B., Béjar, V. J. S., Pérez-Garrido, A., et al. 2015a, ApJ, 804, 96

Gauza, B., Béjar, V. J. S., Rebolo, R., et al. 2015b, MNRAS, 452, 1677
Gray, D. F., & Baliunas, S. L. 1995, ApJ, 441, 436
Hagelberg, J., Engler, N., Fontanive, C., et al. 2020, A&A, 643, A98
Haghighipour, N. 2015, in Encyclopedia of Astrobiology, ed. M. Gargaud et al. (Berlin: Springer), 1942
Hansen, B. M. S., & Murray, N. 2015, MNRAS, 448, 1044
Hawley, S. L., Davenport, J. R. A., Kowalski, A. F., et al. 2014, ApJ, 797, 121
Hełminiak, K. G., Konacki, M., Kulkarni, S. R., & Eisner, J. 2009, MNRAS, 400, 406
Henry, T. J., Ianna, P. A., Kirkpatrick, J. D., & Jahreiss, H. 1997, AJ, 114, 388
Henry, T. J., Jao, W.-C., Subasavage, J. P., et al. 2006, AJ, 132, 2360
Henry, T. J., Jao, W.-C., Winters, J. G., et al. 2018, AJ, 155, 265
Holman, M. J., & Wiegert, P. A. 1999, AJ, 117, 621
Howard, A. W., Marcy, G. W., Fischer, D. A., et al. 2014, ApJ, 794, 51
Janson, M., Quanz, S. P., Carson, J. C., et al. 2015, A&A, 574, A120
Jarrett, T. H., Cohen, M., Masci, F., et al. 2011, ApJ, 735, 112
Johnson, J. A., Aller, K. M., Howard, A. W., & Crepp, J. R. 2010, PASP, 122, 905
Kervella, P., Arenou, F., Mignard, F., & Thévenin, F. 2019, A&A, 623, A72
Kervella, P., Mérand, A., Pichon, B., et al. 2008, A&A, 488, 667
Kiraga, M., & Stepien, K. 2007, AcA, 57, 149
Knapp, W., & Nanson, J. 2018, JDSO, 14, 3
Knutson, H. A., Fulton, B. J., Montet, B. T., et al. 2014, ApJ, 785, 126
Kopparapu, R. k., Wolf, E. T., Haqq-Misra, J., et al. 2016, ApJ, 819, 84
Lafrenière, D., Doyon, R., Marois, C., et al. 2007, ApJ, 670, 1367
Lannier, J., Delorme, P., Lagrange, A. M., et al. 2016, A&A, 596, A83
Launhardt, R., Henning, T., Quirrenbach, A., et al. 2020, A&A, 635, A162
Leggett, S. K., Saumon, D., Marley, M. S., et al. 2012, ApJ, 748, 74
Lestrade, J. F., Wyatt, M. C., Bertoldi, F., Dent, W. R. F., & Menten, K. M. 2006, A&A, 460, 733
Liebert, J., Young, P. A., Arnett, D., Holberg, J. B., & Williams, K. A. 2005, ApJL, 630, L69
Lodieu, N., Pérez-Garrido, A., Béjar, V. J. S., et al. 2014, A&A, 569, A120
Luhman, K. L. 2014, ApJL, 786, L18
Luhman, K. L., & Esplin, T. L. 2016, AJ, 152, 78
Lurie, J. C., Davenport, J. R. A., Hawley, S. L., et al. 2015, ApJ, 800, 95
MacDonald, J., Mullan, D. J., & Dieterich, S. 2018, ApJ, 860, 15
Mamajek, E. E., & Hillenbrand, L. A. 2008, ApJ, 687, 1264
Mann, A. W., Feiden, G. A., Gaidos, E., Boyajian, T., & von Braun, K. 2015, ApJ, 804, 64
Marcy, G. W., Butler, R. P., Fischer, D., et al. 2001, ApJ, 556, 296
Marcy, G. W., Butler, R. P., Vogt, S. S., Fischer, D., & Lissauer, J. J. 1998, ApJL, 505, L147
Marois, C., Macintosh, B., Barman, T., et al. 2008, Sci, 322, 1348
Masset, F. S., & Papaloizou, J. C. B. 2003, ApJ, 588, 494
Mawet, D., Hirsch, L., Lee, E. J., et al. 2019, AJ, 157, 33
McCarthy, D. W., J., Henry, T. J., Fleming, T. A., et al. 1988, ApJ, 333, 943
Meshkat, T., Kenworthy, M. A., Reggiani, M., et al. 2015, MNRAS, 453, 2533
Millholland, S., Laughlin, G., Teske, J., et al. 2018, AJ, 155, 106
Moe, M., & Kratter, K. M. 2021, MNRAS, 507, 3593
Montet, B. T., Crepp, J. R., Johnson, J. A., Howard, A. W., & Marcy, G. W. 2014, ApJ, 781, 28
Morales, J. C., Mustill, A. J., Ribas, I., et al. 2019, Sci, 365, 1441
Murakami, H., Baba, H., Barthel, P., et al. 2007, PASJ, 59, S369
Nakajima, T., Oppenheimer, B. R., Kulkarni, S. R., et al. 1995, Natur, 378, 463
Naoz, S. 2016, ARA&A, 54, 441
Ngo, H., Knutson, H. A., Hinkley, S., et al. 2016, ApJ, 827, 8
Nielsen, E. L., & Close, L. M. 2010, ApJ, 717, 878
Nielsen, E. L., De Rosa, R. J., Macintosh, B., et al. 2019, AJ, 158, 13
Oppenheimer, B. R., Golimowski, D. A., Kulkarni, S. R., et al. 2001, AJ, 121, 2189
Pavlenko, Y. V., Jones, H. R. A., Lyubchik, Y., Tennyson, J., & Pinfield, D. J. 2006, A&A, 447, 709
Pinamonti, M., Damasso, M., Marzari, F., et al. 2018, A&A, 617, A104
Piskorz, D., Knutson, H. A., Ngo, H., et al. 2015, ApJ, 814, 148
Pozuelos, F. J., Suárez, J. C., de Elía, G. C., et al. 2020, A&A, 641, A23
Quanz, S. P., Crossfield, I., Meyer, M. R., Schmalzl, E., & Held, J. 2015, IJAsB, 14, 279
Reiners, A., Schmitt, J. H. M. M., & Liefke, C. 2007, A&A, 466, L13
Reiners, A., Zechmeister, M., Caballero, J. A., et al. 2018, A&A, 612, A49
Reylé, C., Jardine, K., Fouqué, P., et al. 2021, A&A, 650, A201
Ribas, I., Tuomi, M., Reiners, A., et al. 2018, Natur, 563, 365
Rivera, E. J., Laughlin, G., Butler, R. P., et al. 2010, ApJ, 719, 890
Robertson, P., Stefansson, G., Mahadevan, S., et al. 2020, ApJ, 897, 125
Rosenthal, L. J., Fulton, B. J., Hirsch, L. A., et al. 2021, ApJS, 255, 8
Sabotta, S., Schlecker, M., Chaturvedi, P., et al. 2021, A&A, 653, A114
Skemer, A. J., & Close, L. M. 2011, ApJ, 730, 53
Skemer, A. J., Morley, C. V., Zimmerman, N. T., et al. 2016, ApJ, 817, 166
Southworth, J., Bohn, A. J., Kenworthy, M. A., Ginski, C., & Mancini, L. 2020, A&A, 635, A74
Stock, S., Nagel, E., Kemmer, J., et al. 2020a, A&A, 643, A112
Stock, S., Kemmer, J., Reffert, S., et al. 2020b, A&A, 636, A119
Stone, J. M., Skemer, A. J., Hinz, P. M., et al. 2018, AJ, 156, 286
Suárez Mascareño, A., Rebolo, R., González Hernández, J. I., & Esposito, M. 2015, MNRAS, 452, 2745
Suárez Mascareño, A., Rebolo, R., González Hernández, J. I., & Esposito, M. 2017, MNRAS, 468, 4772
Suárez Mascareño, A., Rebolo, R., González Hernández, J. I., et al. 2018, A&A, 612, A89
Telesco, C. M., Packham, C., Ftaclas, C., et al. 2008, Proc. SPIE, 7014, 70140R
Thebault, P., & Haghighipour, N. 2015, in Planetary Exploration and Science: Recent Results and Advances, ed. S. Jin, N. Haghighipour, & W. H. Ip (Berlin: Springer), 309
Trifonov, T., Kürster, M., Zechmeister, M., et al. 2018, A&A, 609, A117
Tuomi, M., Jones, H. R. A., Jenkins, J. S., et al. 2013, A&A, 551, A79
Uyama, T., Hashimoto, J., Kuzuhara, M., et al. 2017, AJ, 153, 106
Vigan, A., Bonavita, M., Biller, B., et al. 2017, A&A, 603, A3
Vigan, A., Fontanive, C., Meyer, M., et al. 2021, A&A, 651, A72
Wang, J., Fischer, D. A., Horch, E. P., & Xie, J.-W. 2015, ApJ, 806, 248
Wargelin, B. J., Kashyap, V. L., Drake, J. J., García-Alvarez, D., & Ratzlaff, P. W. 2008, ApJ, 676, 610
Winn, J. N., & Fabrycky, D. C. 2015, ARA&A, 53, 409
Wittenmyer, R. A., Endl, M., Cochran, W. D., et al. 2006, AJ, 132, 177
Wittenmyer, R. A., Butler, R. P., Tinney, C. G., et al. 2016, ApJ, 819, 28
Wittenmyer, R. A., Wang, S., Horner, J., et al. 2020, MNRAS, 492, 377
Woitas, J., Leinert, C., Jahreiß, H., et al. 2000, A&A, 353, 253
Wright, E. L., Eisenhardt, P. R. M., Mainzer, A. K., et al. 2010, AJ, 140, 1868
Yee, S. W., Petigura, E. A., & von Braun, K. 2017, ApJ, 836, 77
Zechmeister, M., Dreizler, S., Ribas, I., et al. 2019, A&A, 627, A49